

New Approach to Modeling a planar flexible continuum robot simulating elephant trunk

Mahfoudi Chawki^a, Amouri Ammar^{b,c} and Zaatri Abdelouahab^c

^a Department of Mechanical Engineering, University Labri Ben M' Hidi Oum el Bouaghi.
c_mahfoudi_dz@yahoo.fr

^b Welding and NDT Research Centre (CSC), BP 64 Cheraga - Algeria. ammar_ammouri@yahoo.fr

^c Department of Mechanical Engineering, University Mentouri Constantine. azaatri@yahoo.com

Received: 22 October 2013, revised: 01 December 2013, accepted: 21 December 2013

Abstract

Research on the modeling of continuum robots is focused on ways to construct the geometric models, while maintaining maximum specificities and mechanical properties of the robot. This paper presents a new approach of geometric modeling of continuum planar multi-sections robots, assuming that each section is curved in a circular arc, while having inextensible central axis of the structure. The direct geometric model is calculated analytically, whereas the extreme points (used in calculating the inverse geometric model) of each section are calculated numerically using a particle swarm optimization (PSO) method. One advantage of this method is to simplify the mathematical calculations and transform the complex problem into a simple numerical function; which allows the knowledge of the form of the central axis of the robot. Simulation examples using this method are carried to validate the proposed approach.

Keywords: flexible continuum robot; central axis; PSO; Khalil Klifinger method.

1. Introduction

Modeling continuum robots requires a continuous model of the central axis of the robot [1]. Traditional approaches to modeling, in which the frames are associated with each joint, are inappropriate for the case of continuum manipulators, precisely because of the absence of discrete links in their architecture. A natural approach is to use a theoretical curve to model the axis of hyper-redundant robot. The fundamental question, concerning the modeling of the continuum robots, resides also in the infinity of the number of degrees of freedom which require the geometrical models in their continuous form.

However, the hyper-redundant robotic systems (figure 1), with discrete links or continuum cannot be controlled only considering a finite number of degrees of freedom. Thus admitting a reduced set of physical solutions. Among contributions on the geometric models of these structures, we can cite the model of [2, 3] use the Frenet-Serret formulas and modelise the central axis of the robot by a kinematic chain consisting of several rigid bodies.

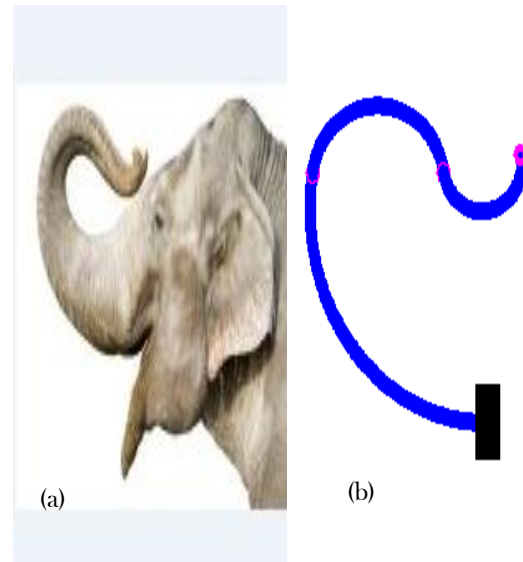


Figure 1: Simulation of the elephant's trunk; (a): the elephant's trunk. (b): the central axis of the robot

[4, 5] assume that each section of a manipulator bends in an arc of a circle and that the central axis of the structure is inextensible. [5] Is based on modified Denavit-Hartenberg convention, the validation of this model has been done on a prototype robot called the ‘elephant trunk’. Similarly [6] uses this assumption to study the kinematics of a snake robot. Furthermore, the inverse geometric model for the case of a multi-section is studied by [8], where the end points of each section are assumed to be known. The authors did not validate experimentally the model but they simulated the overall behavior using appropriate software. [9] Deals with the validation of the geometric model of a multi-section manipulator support by a mobile robot. [10] Has done enhancements on the inverse geometric model described by [4] for one bending section, the validation of this model has done on a micro-robot and showed that the model was not robust against uncertainties of environment and inaccuracies of materials. This inverse geometric model is formulated as an optimization problem with a cost function and constraints using the principle of interval analysis. Finally, a state of the art report in modeling these classes of robots is presented by [11]. The main contribution of this paper is described in two parts. The first presents the methodology follows to know the shape of the central axis of the robot, which represents the direct geometric model. This method relies on the assumption of a constant curvature and is based on knowledge of the angles between the end points of each section constituting the robot; these points will be determined by simple geometrical relations. The second part describes the inverse geometric model; where the extremes points of each section are calculated numerically by using optimization method, under the constraints of conservation of the length of each section. These geometric models presented are used to develop the kinematic and dynamic models for multi-section continuum robot.

2. Direct Geometric Model

2.1. Problem statement

The direct geometric model consists of calculating the position and orientation of the platform n , with respect the base reference, depending on the lengths of cables (or tubes). In what follows, let us assume that each segment is curved in an arc of a circle, and that the central axis of the structure is inextensible. The first tangent of

the curve is collinear with the initial ordered axis of each section (physical stress).

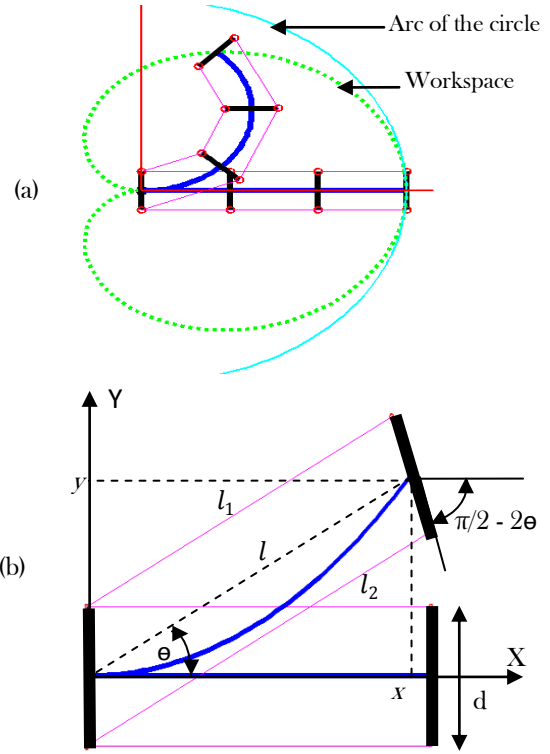


Figure 2: Geometrical parameters (a) Overview of the bending section; (b) A portion of the bending section.

Starting from the definition of arc length, where the curve is described with the arc length parameter: $f(s) = (x(s), y(s))$, then its derivative is a unit vector, so it can be set as a function of an angle $\alpha(s)$ [12]:

$$\dot{f}(s) = \begin{pmatrix} \dot{x}(s) = \cos(\alpha(s)) \\ \dot{y}(s) = \sin(\alpha(s)) \end{pmatrix} \quad (1)$$

From the figure 2(b) we have:

$$\begin{cases} x = l \cos(\theta) = l_1 \cos(\theta) + \frac{d}{2} \sin(2\theta) \\ \quad = l_2 \cos(\theta) - \frac{d}{2} \sin(2\theta) \\ y = l \sin(\theta) = \frac{d}{2} + l_1 \sin(\theta) - \frac{d}{2} \cos(2\theta) \\ \quad = -\frac{d}{2} + l_2 \sin(\theta) + \frac{d}{2} \cos(2\theta) \end{cases} \quad (2)$$

From equation (2) we find:

$$\sin(\theta) = \frac{l_2 - l_1}{2d} \quad (3)$$

$$\cos(\theta) = \sqrt{1 - \left(\frac{l_2 - l_1}{2d}\right)^2} \quad (4)$$

Therefore:

$$\theta = \text{atan2}\left(\frac{l_2 - l_1}{2d}, \sqrt{1 - \left(\frac{l_2 - l_1}{2d}\right)^2}\right) \quad (5)$$

2.2. Calculating the angles function

Consider an inextensible section of length l , formed of $(n + 1)$ points (figure3). When using the arc length, the variation of angles $\alpha(s_i)$ is given by:

$$\alpha(s_i) = As_i + B ; i = 0, 1 \dots n \quad (6)$$

With the boundary conditions:

$$\begin{cases} \alpha(s_0 = 0) = 0 \\ \alpha(s_n = l) = 2\theta \end{cases} \quad (7)$$

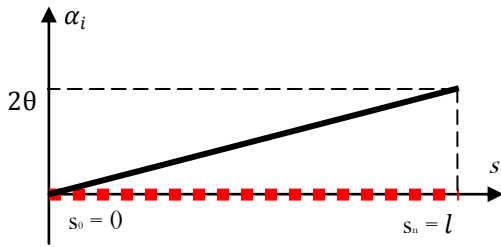


Figure 3: Variation of $\alpha(s)$

After the development we find the expression of $\alpha(s_i)$:

$$\alpha(s_i) = \frac{2\theta}{l} s_i ; s_i \in [0, l] \quad (8)$$

The equation (8) becomes:

$$\alpha(s_i) = \frac{2}{l} \text{atan2}\left(\frac{l_2 - l_1}{2d}, \sqrt{1 - \left(\frac{l_2 - l_1}{2d}\right)^2}\right) s_i \quad (9)$$

2.3. Interpolation of the angles function

The interpolation of the function (9), with a natural cubic spline, gives:

$$\alpha(s) = a_i \left(\frac{s - s_i}{h_i}\right)^3 + b_i \left(\frac{s - s_i}{h_i}\right)^2 + c_i \left(\frac{s - s_i}{h_i}\right)^1 + d_i \quad (10)$$

Where: a_i, b_i, c_i et d_i are parameters of the cubic spline, with $s_i \leq s \leq s_{i+1}$, $h_i = s_{i+1} - s_i$ and $i = 0, \dots, n - 1$.

The constraints of the natural cubic spline are:

- Interpolation at the points:

$$\alpha(s_i^+) = \alpha_i, \quad i = 0, \dots, n - 1$$

$$\alpha(s_i^-) = \alpha_i, \quad i = 1, \dots, n$$
- Continuity C^1 :

$$\alpha'(s_i^+) = \alpha'(s_i^-), \quad i = 1, \dots, n - 1$$
- Continuity C^2 :

$$\alpha''(s_i^+) = \alpha''(s_i^-), \quad i = 1, \dots, n - 1$$
- Minimization of energy:

$$\alpha''(0) = 0 \quad \text{et} \quad \alpha''(l) = 0$$

2.4. Integration of the angles function

Once the function of the angles $\alpha(s)$ determined, we can find the solution by integration of the equation (1), by using Simpson's numerical method. The function solution represents the shape of the central axis of the robot:

$$f(s) = \begin{cases} x(s) = \int_0^s \cos(\alpha(s)) \\ y(s) = \int_0^s \sin(\alpha(s)) \end{cases} \quad (11)$$

2.5. Applications

a. One section

Consider a bending section of length $l = 200 \text{ mm}$. Increasing l_1 and l_2 with $\Delta l = 0:10:30$, such as: $l_1 = l - \Delta l$ and $l_2 = l + \Delta l$. The robot configuration is shown in figure 4 and the curves of the associated angles functions of each movement are shown in figure 5. The position and orientation of the superior platform with respect to base reference is given by equations (11) and (5) for $s = l$.

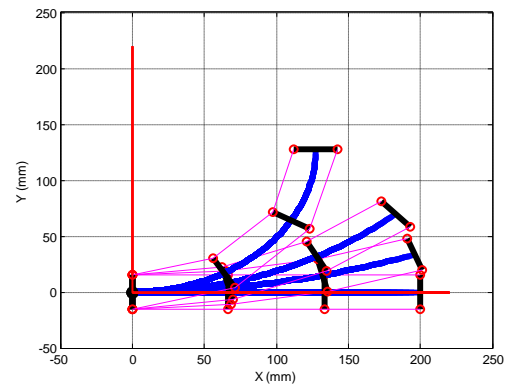


Figure 4: Planar robot with a single section

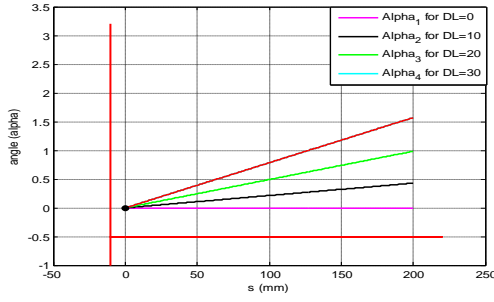


Figure 5: Functions of the associated angles

b. Three sections

Consider a robot formed with three sections of length $l_1 = 200 \text{ mm}$, $l_2 = 150 \text{ mm}$ and $l_3 = 100 \text{ mm}$. The position and orientation of the platform j with respect to base reference for a variation of the cables $l_{i,j}$ ($l_{1,1} = 170, l_{2,1} = 230, l_{1,2} = 170, l_{2,2} = 130, l_{1,3} = 130, l_{2,3} = 70$); is given by equations (11) and (5)

- Platform 1: $\begin{cases} f(l_1) = \begin{cases} x_1 = 165.40 \\ y_1 = 95.49 \end{cases} \\ \theta_1 = \pi/3 \end{cases}$
- Platform 2: $\begin{cases} f(l_1 + l_2) = \begin{cases} x_2 = 294.05 \\ y_2 = 133.97 \end{cases} \\ \theta_2 = -0.486 \end{cases}$
- Platform 3: $\begin{cases} f(l_1 + l_2 + l_3) = \begin{cases} x_3 = 382.77 \\ y_3 = 158.08 \end{cases} \\ \theta_3 = \pi/3 \end{cases}$

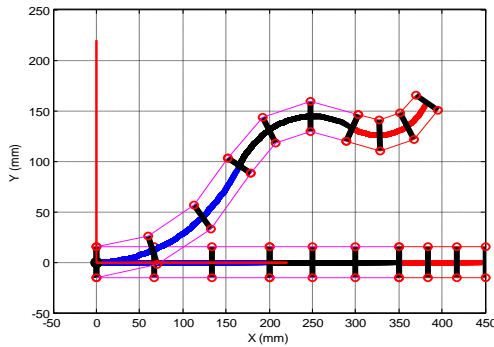


Figure 6: Initial and final position of the robot with three bending sections

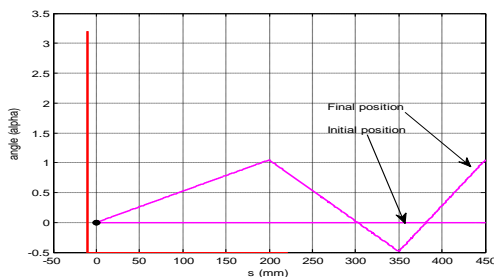


Figure 7: The function of the associated angles

3. Inverse geometric model

3.1. Inverse geometric model for one section

One bending section of a continuum manipulator is modeled by an arc of circle with one end point o fixed at the origin of the reference frame; the other end point P is located anywhere in the workspace. This section of continuum manipulator is parameterized by lengths, its curvature κ , and its orientation θ as shown in figure 8. These parameters are given by:

$$\theta = \text{atan2}(y, x) \quad (12)$$

$$\kappa = \sqrt{\frac{2(1 - \cos(2\theta))}{x^2 + y^2}} \quad (13)$$

$$s = \frac{2\theta}{\kappa} \quad (14)$$

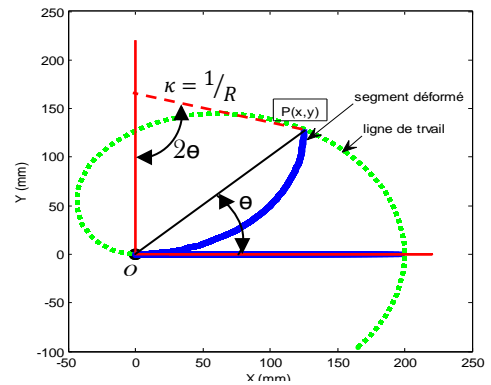


Figure 8: Circle arc parameters

3.2. Inverse geometric model for multi-sections

The inverse geometric model presented in the previous section can be iteratively applied to several sections in serial connection to model a continuum manipulator of n sections.

The operational coordinates of the origins of the intermediate platforms (x_i, y_i) of each sections, are calculated numerically by the PSO method, using constraints on the conservation length, such that $l_i = \sqrt{((x_i - x_{i-1})^2 + (y_i - y_{i-1})^2)} \theta_i / \sin(\theta_i)$, with $\theta_i = \text{atan2}((y_i - y_{i-1}), (x_i - x_{i-1}))$, for $i = 1, \dots, n$. Where (x_i, y_i) are the Cartesian coordinates of the origin of reference frame R_i in the frame R_{i-1} . The algorithm for computing the inverse geometric model of the overall structure is presented in figure 9.

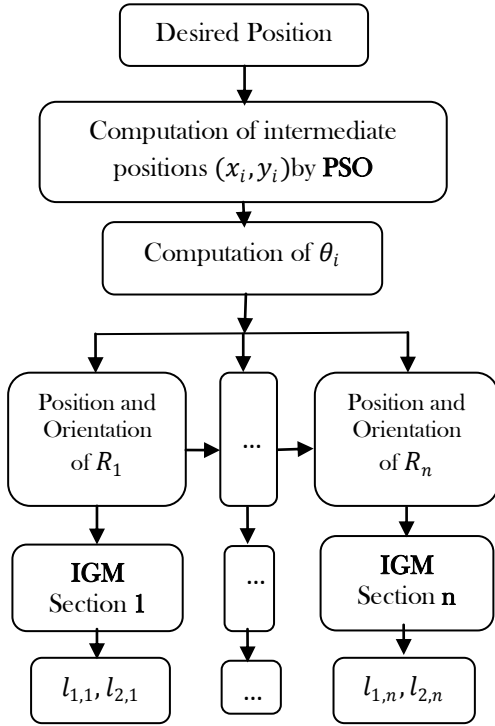


Figure 9: Algorithm for computing the inverse geometric model of a *planar flexible continuum robot*

This optimization method is inspired by the social behavior of some biological organisms, especially the group's ability of some animal species to locate a desirable position in the given area. This method uses the simple rules of displacement in the space of the solutions, where the particles can progressively converge to a local minimum. For each iteration t , the velocity changes by applying equation (15) to each particle.

$$v_i(t+1) = \omega v_i(t) + c_1 \varphi_1 (P_{ibest} - x_i) + c_2 \varphi_2 (P_{gbest} - x_i) \quad (15)$$

$$x_i(t+1) = x_i(t) + v_i(t+1) \quad (16)$$

Where ω is called the inertia weight, c_1 and c_2 are weighting factors and φ_1 , φ_2 are random variables uniformly distributed within interval $[0, 1]$. P_{ibest} and P_{gbest} represent the best position visited by a particle and the best position visited by the swarm till the current iteration t . The position update is applied by equation (16) based on the new velocity and the current position. The calculation steps are given by the following algorithm:

- For the time step t
- For each particle
- For each dimension d

$$\text{Modify the velocity:}$$

$$\begin{cases} v_d(t+1) = \omega v_d(t) + \\ \text{aleatory.}[c_1 \varphi_1](P_{i,d} - x_d(t)) + \\ \text{aleatory.}[c_2 \varphi_2](P_{g,d} - x_d(t)) \end{cases}$$

$$\text{- Move: } x(t+1) = x(t) + v(t+1)$$

3.3. Application

Knowing the general movement of the platform n generated by the operational coordinates (x_n, y_n) we determine the displacements of the actuators and the mobile platforms. To illustrate this inverse geometric modeling, we applied it on a planar robot consisting of two bending sections of length $l_1 = 140 \text{ mm}$ and $l_2 = 120 \text{ mm}$, for the following settings of the trajectory in operational space:

$$\begin{cases} x_2 = 260 - 15 \times t \\ y_2 = 15 \times t \end{cases}$$

Where t is time variable varying from 0 to 8 sec, with a step equal 2 sec .

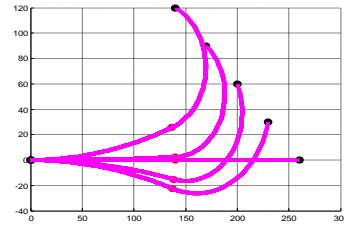


Figure 10: The virtual axis of the robot

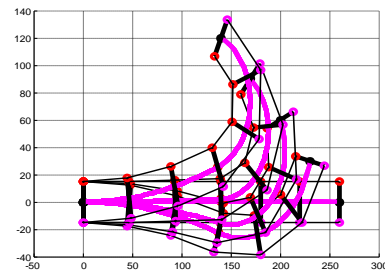


Figure 11: Robot with two bending sections describing a linear path

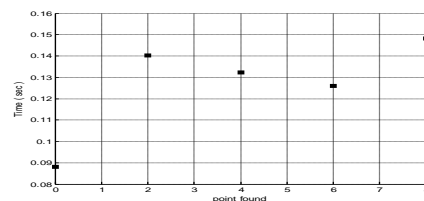


Figure 12: The execution time of the optimization algorithm for each point found.

The simulations were done on a PC with a processor i3 3.30 GHz. the execution time of the optimization process for each point found is shown in figure.12. The average time is equal to 0.128 sec.

Conclusion and future works

In this paper, a new approach of modeling of the planar flexible continuum robots is presented. We have detailed the methodology to formulate the function describing the curvature of the central axis of the robot. The principal idea of our work is based on rebuilding of curves work starting from the tangential data developed in [12]. Mathematical formulations of a planar continuum robot are given; these formulations provide the calculation of the cables lengths of the robot for of a given point in the workspace and vice versa. The operational coordinates of the intermediate platforms origins, used in the calculation of the inverse geometric model, are calculated by a numerical method where the space of search for this method is arbitrarily selected. Future work is to improve the execution time, one taking the space of research in the workspace of each section, in order to find a solution close to real time. To have the uniqueness of the solution the introduction of other constraints is necessary. Also the generalization of the approach in the three-dimensional is projected.

References

- [1] L. Fryziel, "Modélisation et calibrage pour la commande d'un micro-robot continuum dédié à la chirurgie mini-invasive", Thesis of Doctorate of the University Paris Est Créteil Val de Marne. June 2011.
- [2] H. Mochiyama, E. Shimemura and H. Kobayashi, Shape correspondence between a spatial curve and a manipulator with hyper degrees of freedom, In Proc. of IEEE/RSJ, vol. 1, 13-17 October 1998, Victoria, BC, Canada, pp.161-166.
- [3] H. Mochiyama and T. Suzuki, "Kinematics and dynamics of a cable-like hyper-flexible manipulator", In Proc. IEEE Int Conf. Robot Automat. Taipei, Taiwan, 2003, vol. 3, pp. 3672-3677.
- [4] M. H. Hannan and I.D. Walker, The 'Elephant Trunk' Manipulator, Design and Implementation, 2001 IEEE/ASME International Conference on Advanced Intelligent Mechatronics Proceedings, 8-12 July 2001, Como, Italy, pp.14-19.
- [5] B. A. Jones, and I. D. Walker, Kinematics for Multisection Continuum Robots, IEEE Transactions on Robotics, vol. 22, No. 1, February 2006, pp 43-55.
- [6] Y. Nakabo, T. Mukai and K. Asaka, Electroactive polymers for robotic applications, London: Springer, Chapter 7, Biomimetic soft robots using IPMC, 2007.
- [7] M. Hannan and I. D. Walker ID, Kinematics and the Implementation of an Elephant's Trunk Manipulator and Other Continuum Style Robots, Journal of Robotic Systems, vol. 20(2), pp. 45-63, 2003.
- [8] S. Neppalli, M. A. Csencsits, B. A. Jones, and I. D. Walker, Closed-Form Inverse Kinematics for Continuum Manipulators, Advanced Robotics 23 (2009), USA, pp. 2077-2091.
- [9] C. Escande, P. M. Pathak, R. Merzouki, V. Coelen, Modeling of Multisection Bionic Manipulator: application to Robotino XT, 2011 IEEE International Conference on Robotics and Biomimetics (ROBIO), 7-11 Dec. 2011, Phuket, Thailand, pp.92-97.
- [10] Iqbal S., Mohammed S., Amirat Y., "A guaranteed approach for kinematic analysis of continuum robot based catheter," International Conference on Robotics and Biomimetics (ROBIO)19-23, Dec 2009 IEEE, France, pp.1573-1578.
- [11] Robert J. Webster III and Bryan A. Jones, Design and Kinematic Modeling of Constant Curvature Continuum Robots: A Review, The International Journal of Robotics Research 29(13), 10 June 2010, USA, pp. 1661-1683.
- [12] N. Sprynski, B. Lacolle, L. Biard, D. David, (2006), Curves and Surfaces Reconstruction via Tangential Informations, Sixth International Conference on Curve and Surface Design, Curve and Surface design, Avignon, July 2006, pp. 254-263.
- [13] J. Kennedy, R. Eberhart, Particle swarm optimization, in: Proc. IEEE Int. Conf. Neural Networks, 1995. p. 1942-1948.
- [14] J. Moore, R. Chapman, Application of Particle Swarm to Multiobjective Optimization, Department of Computer Science and Software Engineering, Auburn University, 1999.

Effect of surfactants in the synthesis of NiO nanoparticles by colloidal thermal assisted reflux condensation method

Mohamed Jaffer Sadiq M^a. and Samson Nesaraj A^{b,*}

^aDepartment of Nanosciences and Technology, Karunya University, Coimbatore – 641 114, India

^bDepartment of Chemistry, Karunya University, Coimbatore – 641 114, India

*email address: drsamson@karunya.edu

Received: 29 August 2013, revised: 26 December 2013, accepted: 27 December 2013

Abstract

Nickel oxide (NiO) nanoparticles were prepared by colloidal thermal assisted reflux condensation method using nickel acetate (precursor salt) and N, N - Dimethylformamide - DMF (solvent) with or without the addition of surfactants such as cetyl trimethyl ammonium bromide (CTAB), polyvinyl pyrrolidone (PVP), polyvinyl alcohol (PVA) and sodium monododecyl sulphate (SDS) respectively. Finally, the prepared samples products were calcined at different temperatures systematically such as at 200°C, 400°C, 600°C, 800°C for 2 hrs each to get the phase pure product. The calcined nanoparticles were characterized by X-Ray Diffraction (XRD), Energy Dispersive X-ray Analysis (EDAX), Fourier Transform Infrared (FTIR) Spectroscopy, Particle Size Analysis, Scanning Electron Microscopy (SEM), Diffuse Reflectance Spectroscopy (DRS) and Photo Luminescence (PL) Spectroscopy techniques. All the samples were crystallized in cubic structure. Effect of surfactants in the synthesis of nickel oxide (NiO) particles is discussed and reported.

Keywords: Thermal assisted reflux condensation method; NiO nanoparticles; Effect of surfactants

1. Introduction

Metal oxide nanoparticles have been studied world-wide for potential applications now-a-days. NiO is a p-type semiconductor oxide material owing to its defect structure and it has a wide band gap energy range from 3.4 - 4 eV [1, 2]. NiO has been studied various groups since it has an excellent durability and electrochemical stability as well due to its good optical, magnetic and electrical characteristics[3-5]. Further, NiO is a potential candidate for various applications such as electronic devices [6-8], catalysts [9-11], smart windows [12], battery electrodes [13], dye-sensitized solar cell devices [14,15], electro chromic display devices and films [16,17], gas sensor materials [18], electrochemical super capacitors [19], antiferro-magnetic films [20], fuel cell electrodes [21,22], energy efficient automobile mirrors [23], building glazing materials [24] and hetero junction solar cells [25]. Several reports showed an amazing level of its performance as a candidate material for various other applications also [26-27]. NiO

nanoparticles were prepared by various routes such as, sputtering [28-31], electrochemical deposition [32-34], thermal decomposition [35-37], electron beam evaporation[38], vacuum evaporation[39], solvothermal[40], polymer-matrix assisted synthesis[41], spray pyrolysis[42,43], surfactant-mediated synthesis[44], sol-gel technique[45-50], chemical method[51], chemical precipitation [52,53], micro emulsion [54], reactive pulsed laser ablation technique [55], hydrothermal method [56-58] microwave method [59], etc. In this research work, we report a simple way of synthesizing NiO nanoparticles by a colloidal thermal assisted reflux condensation method in presence of surfactants. The prepared materials were characterized systematically by XRD, EDAX, FTIR, Particle Size Analysis, SEM, DRS and PL techniques. The effect of surfactants in the synthesis of NiO nanoparticles is discussed and reported.

2. Experimental procedure

The analytical grade chemicals such as nickel acetate (Merck, India), N, N-Dimethylformamide (Merck, India), cetyl trimethyl ammonium bromide (Merck, India), polyvinyl pyrrolidone (Merck, India), polyvinyl alcohol (Merck, India) and sodium monododecyl sulphate (Merck, India), ethanol (Merck, India) were used. Deionized water was used throughout the experiment. The NiO nanoparticles were prepared by colloidal thermal assisted reflux condensation method as shown in Fig. 1. In the typical experiment, the nickel acetate solution (1M) was prepared by dissolving it in 100 ml DMF. The above solution mixture was taken in a RB flask and stirred well at room temperature for about 10 minutes. After stirring, a reflux condenser was connected with the RB flask and the solution was refluxed at 90° C for 6 h in a magnetic stirring apparatus (1200 rpm). A colloidal precipitate was resulted. It was cooled down and the precipitate was separated by centrifugation. The separated precipitate was washed thoroughly with 9:1 water ethanol mixture and then dried at 85° C for 2 h. The resultant material was heat treated at temperatures such as, 200, 400, 600 and 800°C for 2 h each to get a phase pure product. The above experiment was repeated with the addition of surfactant (1 %) such as CTAB, PVP, PVA and SDS each at the initial stage itself to study the effect of surfactants in the preparation of NiO nanoparticles. The reaction and mechanism involved in the synthesis of NiO nanoparticles are indicated in Fig. 2.

The powder XRD studies were carried out with a Shimadzu XRD6000 X-ray diffractometer using CuK α radiation ($\lambda = 0.154059$ nm) radiation with a nickel filter. The applied current and voltage were 30 mA and 40 kV respectively. The 2θ scanning range was 10° to 90° with a scan rate of 10°/min⁻¹. The crystallite sizes of nickel oxide were estimated using the Debye-Scherrer equation. The chemical structure information of NiO nano powder were recorded by Fourier transform infrared spectra (SHIMADZU Spectrophotometer) using KBr pellet technique in the range from 4000cm⁻¹ to 400cm⁻¹ (spectral resolution was 4 cm⁻¹ and number of scans was 20). The average particle size of the NiO nano powder was measured with a Zetasizer Ver. 6.32 manufactured by the Malvern Instruments Ltd. The surface morphology, size of particles and elemental compositions of NiO nano powder was characterized by scanning electron microscope (SEM JEOL JSM-6610) equipped with an energy dispersive X-ray (EDAX) spectrophotometer and operated at 20kV. Absorbance spectra of the NiO nano powder were recorded by UV-Visible Double Beam Spectrophotometer (Shimadzu 1800), equipped with a diffuse reflectance sphere using Teflon was employed as a reference material. Powder samples were loaded into a quartz cell and spectra were recorded range between 200 nm to 600 nm by using

diffused reflectance method. Photoluminescence spectrum of the NiO nano powder was measured by Spectrofluorophotometer (FLUOROLOG, HORIBA YVON) with Xe laser as the excitation light source at room temperature.

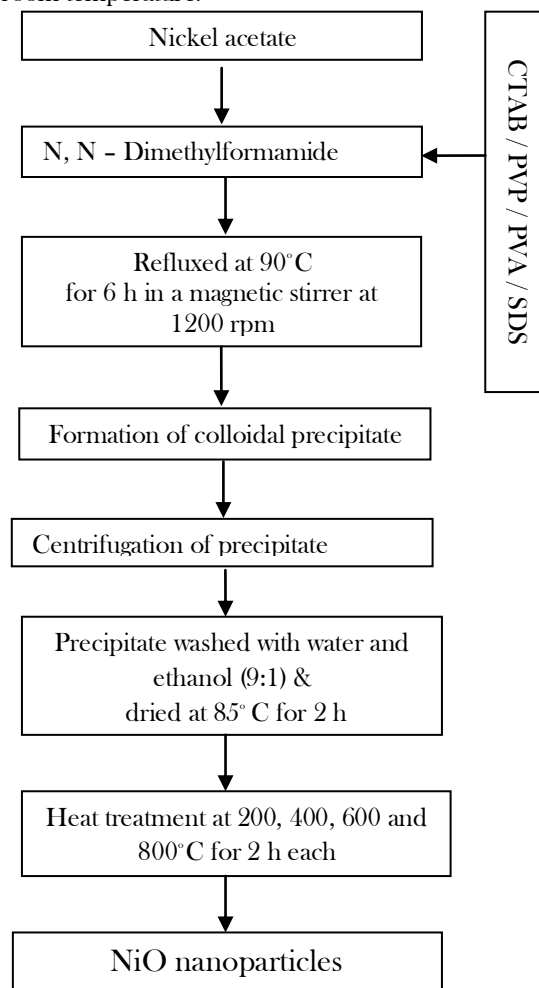


Figure 1. Flow chart to prepare NiO nanoparticles by colloidal thermal assisted reflux condensation method

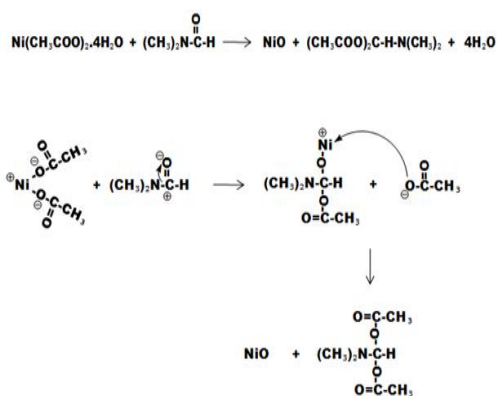


Figure 2. Reaction and mechanism involved in the synthesis of NiO nanoparticles by colloidal thermal assisted reflux condensation method

3. Results & Discussion

3.1. X-Ray Diffraction Studies

The powder XRD patterns obtained on NiO nanoparticles prepared by colloidal thermal assisted reflux condensation method are indicated in Fig. 3. The XRD peaks are found to be very sharp indicating the highly crystalline nature of the sample. The product is identified as NiO using JCPDS pattern No. 01-1239. The diffraction peaks found in all the samples can be exactly indexed to a cubic structure of NiO. The lattice parameters were calculated from 2θ values in the X-ray diffraction patterns. No characteristic peaks of impurity were observed. The crystal size (D_x) was calculated using the Debye-Scherrer formula [60].

$$D_x = 0.91 \lambda / \beta \cos\theta \quad (1)$$

Where ' λ ' is the X-ray wavelength ($\lambda = 0.154059$ nm for CuK α), ' β ' is the FWHM (full width at half maximum intensity) and ' θ ' is the Bragg's angle.

The theoretical density (D_p) was calculated using the formula [61].

$$D_p = (Z * M) / (N * a^3) \text{ g.cm}^{-3} \quad (2)$$

Where ' Z ' is the number of chemical species in the unit cell, ' M ' is the molecular mass of the sample (g/mol), ' N ' is the Avogadro's number (6.022×10^{23}) and ' a ' is the lattice constant (cm). The crystallographic parameters obtained on the NiO nanoparticles are given in the Table 1.

Table 1. The crystallographic parameters obtained on NiO nanoparticles prepared by colloidal thermal assisted reflux condensation method

Sample	Crystal structure	Unit cell lattice parameter 'a' (Å)	Unit cell volume (Å) ³	Theoretical density (g/cc)	Crystallite size (nm)
Standard XRD data for NiO powder (JCPDS No. 01-1239)	Cubic	4.171	72.56	6.838	--
NiO (prepared without any surfactant)	Cubic	4.1786	72.9613	6.7999	.30
NiO (prepared with CTAB)	Cubic	4.1714	72.5848	6.8352	5.17
NiO (prepared with PVP)	Cubic	4.1538	71.6699	6.9225	5.12
NiO (prepared with PVA)	Cubic	4.1600	71.9913	6.8916	4.87
NiO (prepared with SDS)	Cubic	4.1534	71.6492	6.9245	4.55

3.2 Energy dispersive X- ray spectroscopy (EDAX) analysis

The EDAX spectra of NiO nanoparticles synthesized by colloidal thermal assisted reflux condensation method are reported in Fig. 4. EDAX spectra of the samples show peaks for Ni and O only and not for any other impurities in the samples. The chemical composition data obtained on NiO by EDAX analysis is given in Table 2. The data confirmed the presence of nickel and oxygen in all the samples. From the EDAX data, it was found that the weight percentage of nickel is varied between 53.0-57.46 % and for oxygen is 42.54 - 47.0%. The variation in the percentage of elements (Ni and O) may be due to the reaction conditions during the preparation of nickel oxide nanoparticles. EDAX shows that samples 'a' and 'b' are substoichiometric and samples 'c', 'd' and 'e' have an oxygen excess (or a deficit on Ni) which is the case for thermodynamically stable NiO (the departure from stoichiometry in Ni_{1-x}O

is due to nickel vacancies). All these compounds are far from equilibrium. The lattice parameters of samples 'c', 'd' and 'e' are less than samples 'a' and 'b' which also describes the above effect.

3.3 FTIR spectroscopic studies

Fig. 5 shows the FTIR spectra obtained on NiO nanoparticles prepared by colloidal thermal assisted reflux condensation method. FTIR studies were carried out to understand the presence of functional group of any organic molecule. Generally, any metal oxide may show absorption bands below 1000 cm⁻¹ due to inter atomic vibrations. The wide band at 3620 and 1640 cm⁻¹ present in all the samples is mainly due to the stretching vibration mode O-H group, which are associated with the adsorbed water on the products [62]. The broad absorption band in the region of 600 - 700 cm⁻¹ is assigned to Ni-O stretching vibration mode; the broadness of the absorption band indicates that the NiO powers are nanocrystals [63].

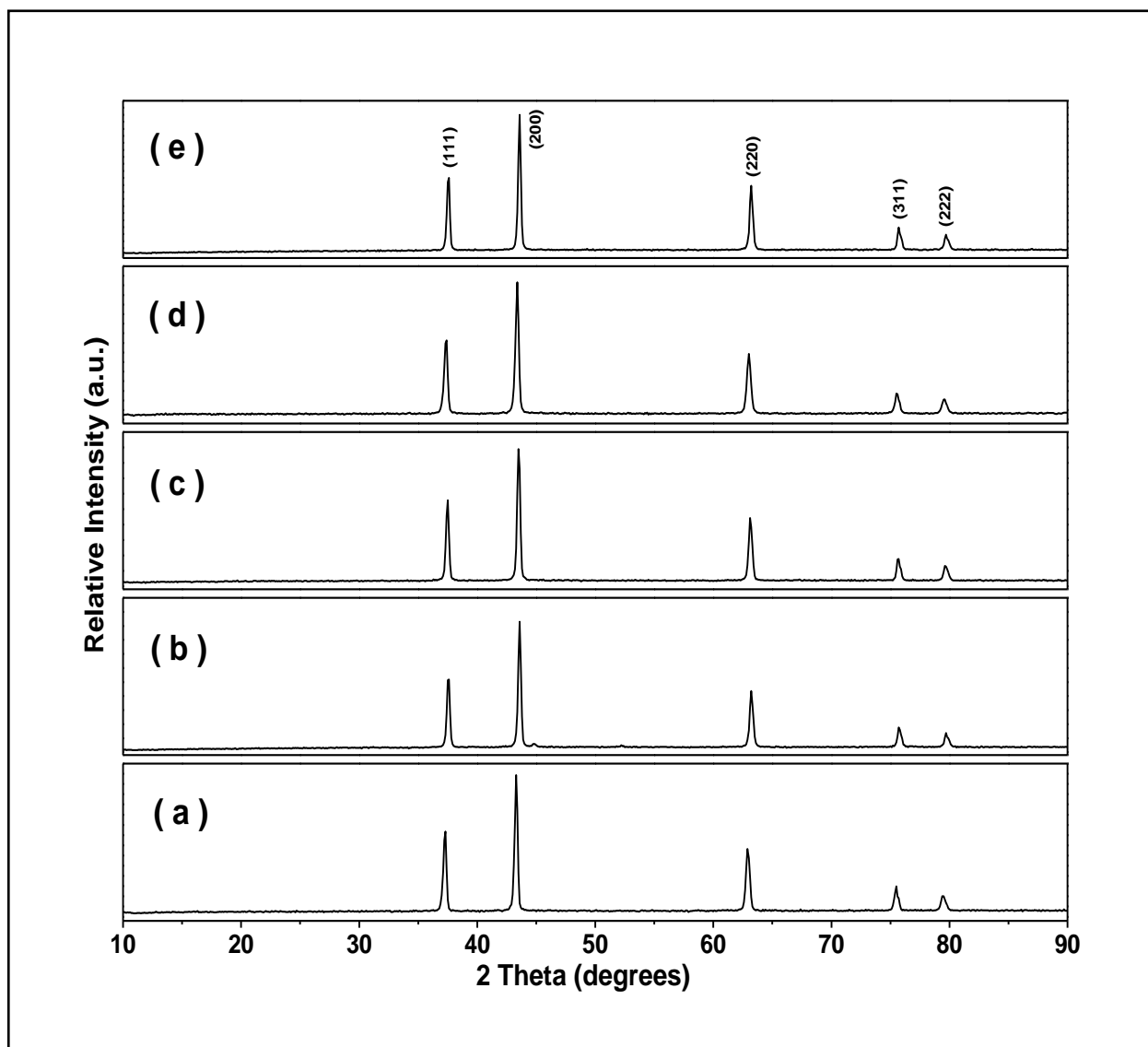


Figure 3. Powder XRD patterns obtained on NiO nanoparticles prepared by colloidal thermal assisted reflux condensation method (a) without any surfactant (b) prepared with CTAB (c) prepared with PVP (d) prepared with PVA (e) prepared with SDS

3.4 Particle size analysis

The particle size distribution curves obtained with NiO nanoparticles prepared by colloidal thermal assisted reflux condensation method are shown in Fig.6. The particle characteristics data obtained on NiO nanoparticles particles is indicated in Table 3. From the particle size distribution data (Table 3), it was found the sample prepared with SDS as a surfactant resulted in very low particle size (78.98 nm). The presence of bigger particles (> 500 nm) in the samples may be due to high temperature treatment. It was reported that the higher temperature caused agglomeration to occur more readily[24]. However,

the results obtained through laser scattering analysis are less reliable than microstructural studies.

3.5 SEM studies

The SEM images of the NiO nanoparticles prepared by colloidal thermal assisted reflux condensation method are indicated in Fig.7. Presence of nanostructural homogeneity in all the samples was confirmed by the SEM photographs. The images indicate that the samples have monodisperse and polycrystalline particles. The particles were spherical in shape and it was observed that some of the particles were agglomerated with each other due to large surface energy and large surface tension of the ultrafine particles. Smaller size grains were present in

the sample prepared with SDS as a surfactant which is in accordance with the particle characteristics data. The samples 'c' and 'e' whose SEM images show large differences in aggregates size and size distributions (Fig. 6) but similar compositions and lattice

parameters. The above difference in the particle characteristics of samples 'c' and 'e' is due to the departure from stoichiometry in Ni_xO and which may be due to nickel vacancies.

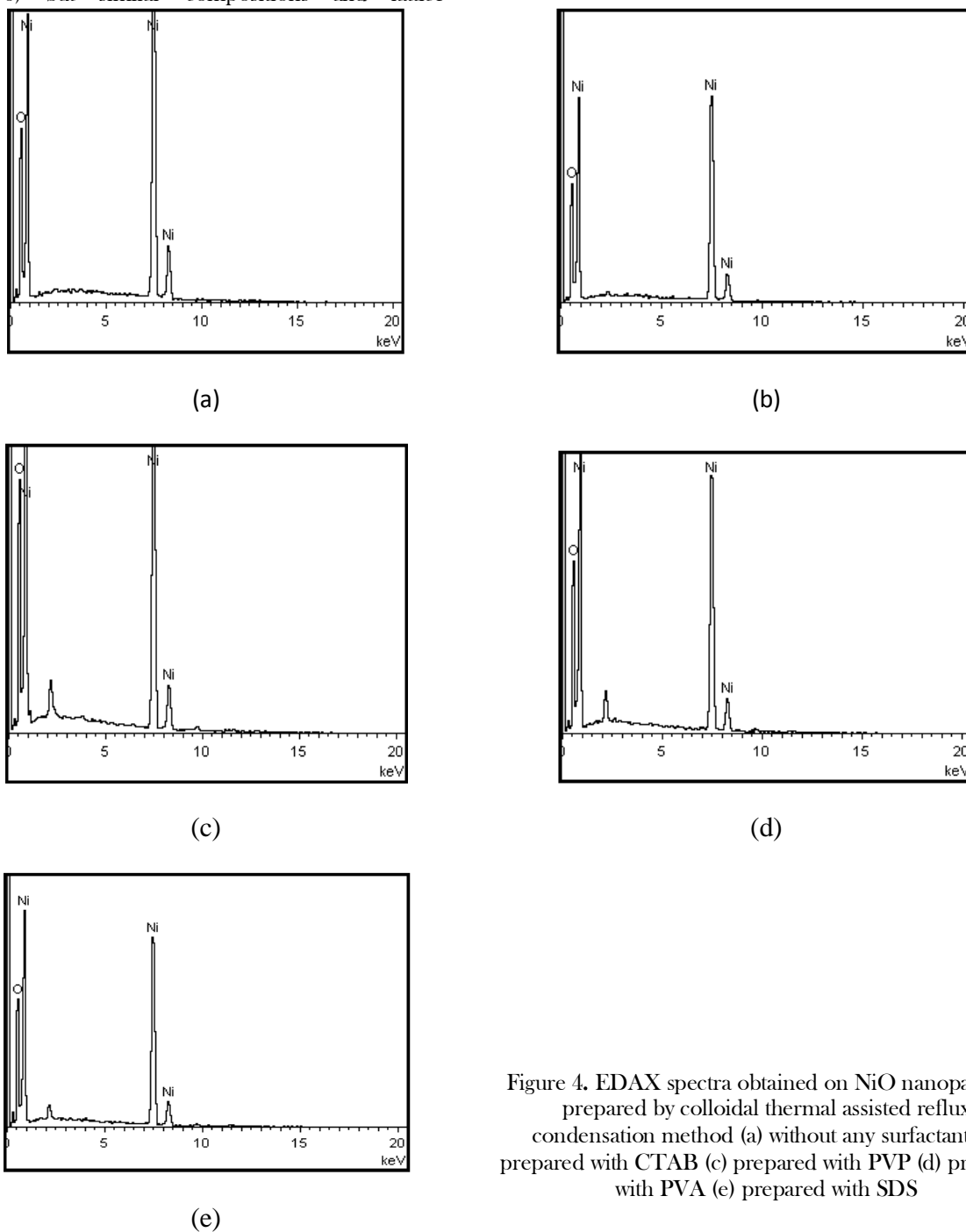


Figure 4. EDAX spectra obtained on NiO nanoparticles prepared by colloidal thermal assisted reflux condensation method (a) without any surfactant (b) prepared with CTAB (c) prepared with PVP (d) prepared with PVA (e) prepared with SDS

3.6. DRS studies

The DRS spectra obtained in all the samples are indicated in Fig.8. The absorption wavelengths of 343, 342, 339, 337 and 336 nm were obtained for NiO nanoparticles prepared by colloidal thermal assisted reflux condensation method without any

surfactants and with surfactants, CTAB, PVP, PVA and SDS respectively. Energy band gap values for all the samples were calculated by using Tauc relation [64].

$$(\alpha h\nu)^n = A (h\nu - E_g) \quad (3)$$

Where ' α ' is the absorption coefficient, ' $h\nu$ ' is the photo energy, ' E_g ' is the optical band gap, ' A ' is a constant relative to the material and ' n ' is either 2 for direct transition, or $\frac{1}{2}$ for an indirect transition. The optical band gap value for the direct transition was obtained from Fig. 9. The calculated band gap values for the NiO nanoparticles were 3.45, 3.52, 3.57, 3.64 and 3.69 eV for the samples prepared without any

surfactant and with surfactants, CTAB, PVP, PVA and SDS respectively. The reported band gap values for the NiO sample are in the range 3.4 - 4.0 eV[2]. Hence, the band gap values calculated for the NiO particles are in agreement with the reported data. The obtained band gap values of NiO nanoparticles may cause a blue shift in their absorption spectra due to quantum confinement effects.

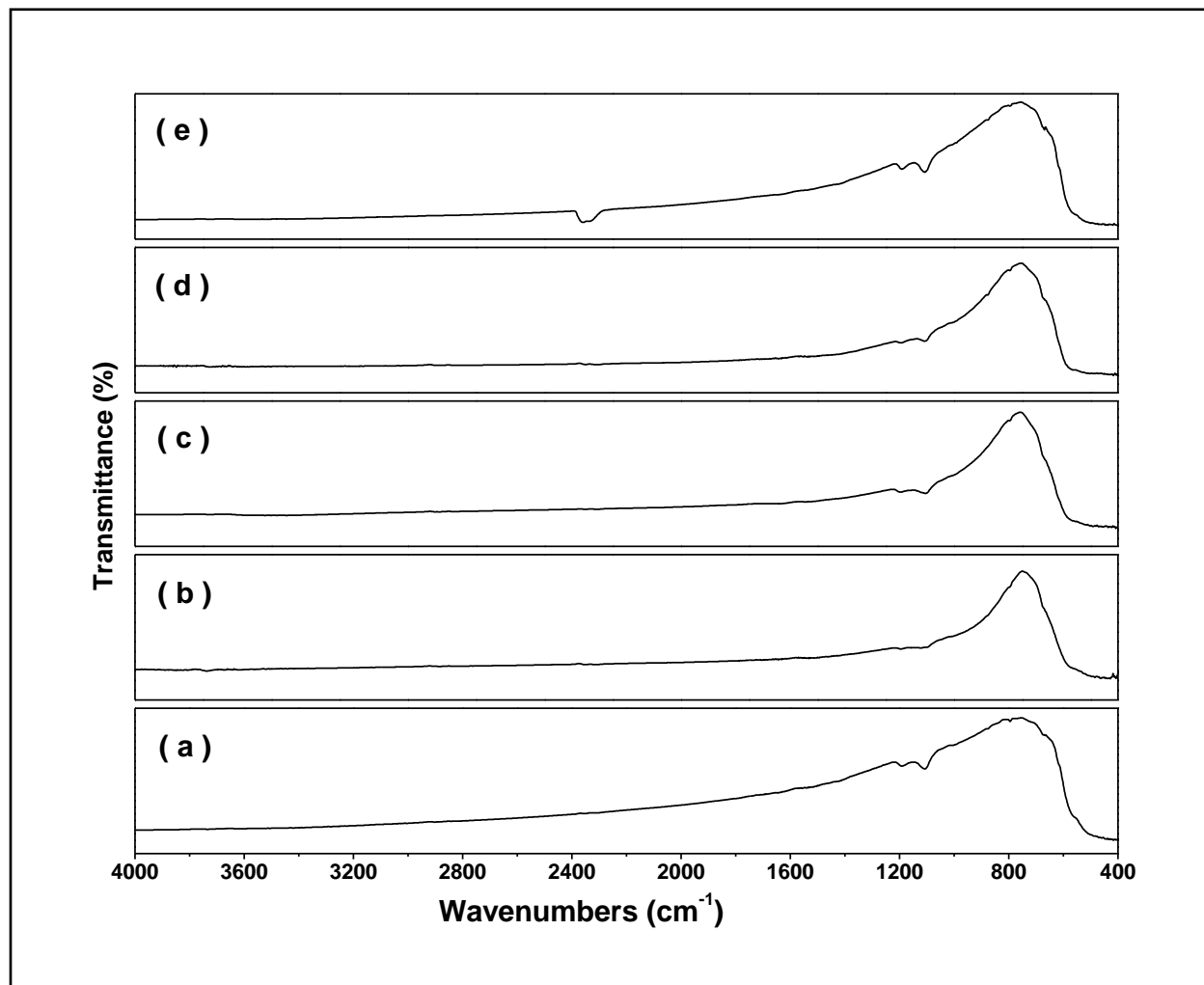


Figure 5. FTIR spectra obtained on NiO nanoparticles prepared by colloidal thermal assisted reflux condensation method (a) without any surfactant (b) prepared with CTAB (c) prepared with PVP (d) prepared with PVA (e) prepared with SDS

3.7. PL emission spectra studies

The PL Emission spectra obtained in all the samples are indicated in Fig.10. The excitation wavelength is 340 nm. A strong PL emission peak was found at 410 nm (3.03 eV) which is corresponding to near emission band edge in all the samples due to the recombination of excitons. The strong PL emission peak is attributed to the high purity and perfect

crystallinity of the NiO nanoparticles. The above result also in accordance with the reported data.

4. Conclusions

NiO nanoparticles are prepared by Colloidal thermal assisted reflux condensation method using various surfactants (CTAB, PVP, PVA and SDS) and the results are reported. The XRD data obtained on NiO nanoparticles shows that all samples crystallized as cubic. The EDAX data confirmed the presence of

nickel and oxygen in all the samples. From the FTIR data, it is shown that all samples exhibited characteristic peaks for NiO and the samples have moisture due to their less size. The particulate properties obtained on NiO powder suggest that the particles are present in the nanometer range. The SEM images exhibit that the samples prepared with the addition of SDS (surfactant) during the preparation of NiO resulted in smaller particle size

than other samples. Optical studies were carried out by DRS spectra and PL emission spectra.

5. Acknowledgment

The authors thank DST Nanomission, Government of India for the financial support. Also, they thank Karunya University for providing all the facilities to carryout nanotechnology research activity in the University campus.

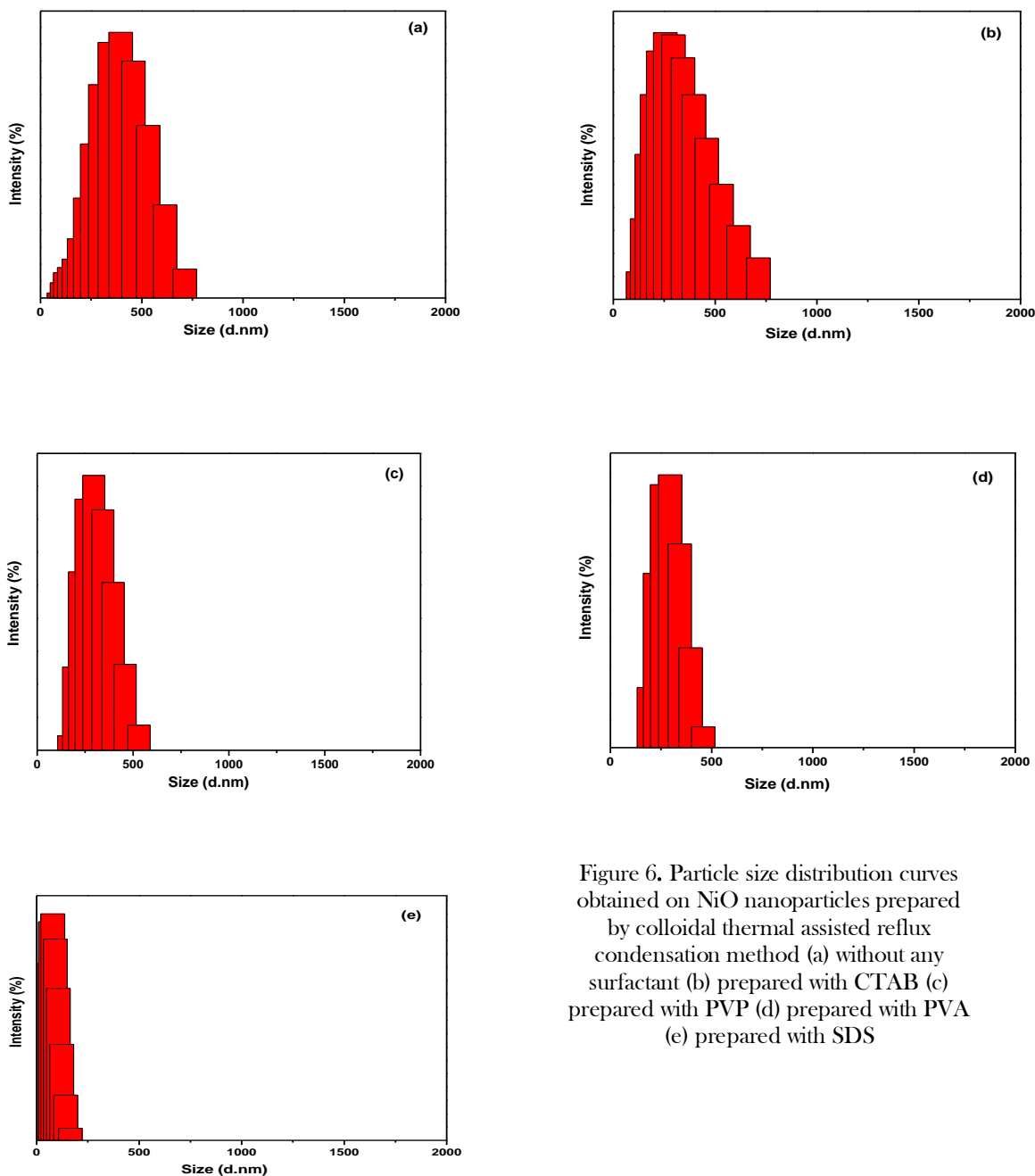


Figure 6. Particle size distribution curves obtained on NiO nanoparticles prepared by colloidal thermal assisted reflux condensation method (a) without any surfactant (b) prepared with CTAB (c) prepared with PVP (d) prepared with PVA (e) prepared with SDS

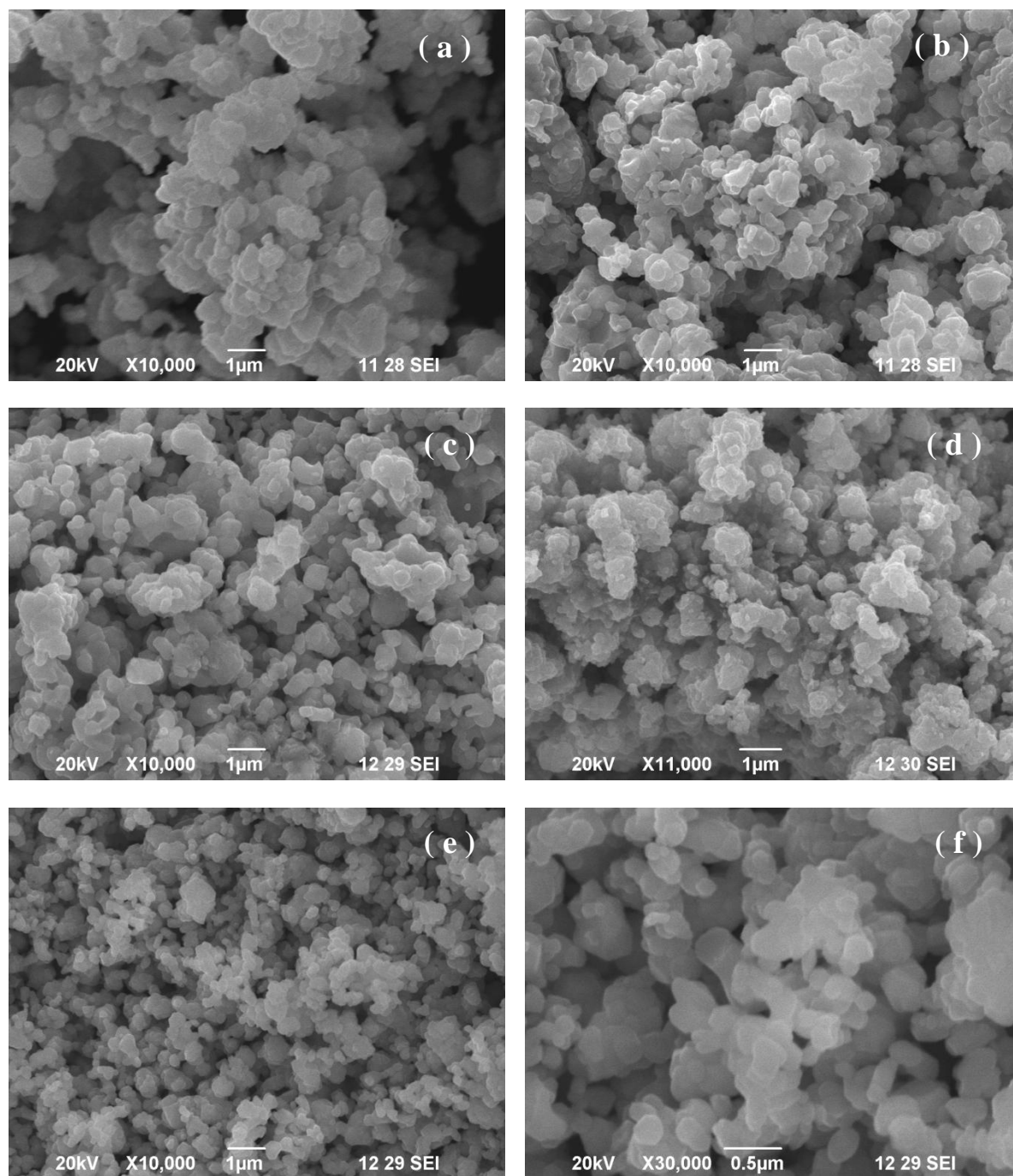


Figure 7. SEM image obtained on NiO nanoparticles prepared by colloidal thermal assisted reflux condensation method (a) without any surfactant (b) prepared with CTAB (c) prepared with PVP (d) prepared with PVA (e) & (f) prepared with SDS

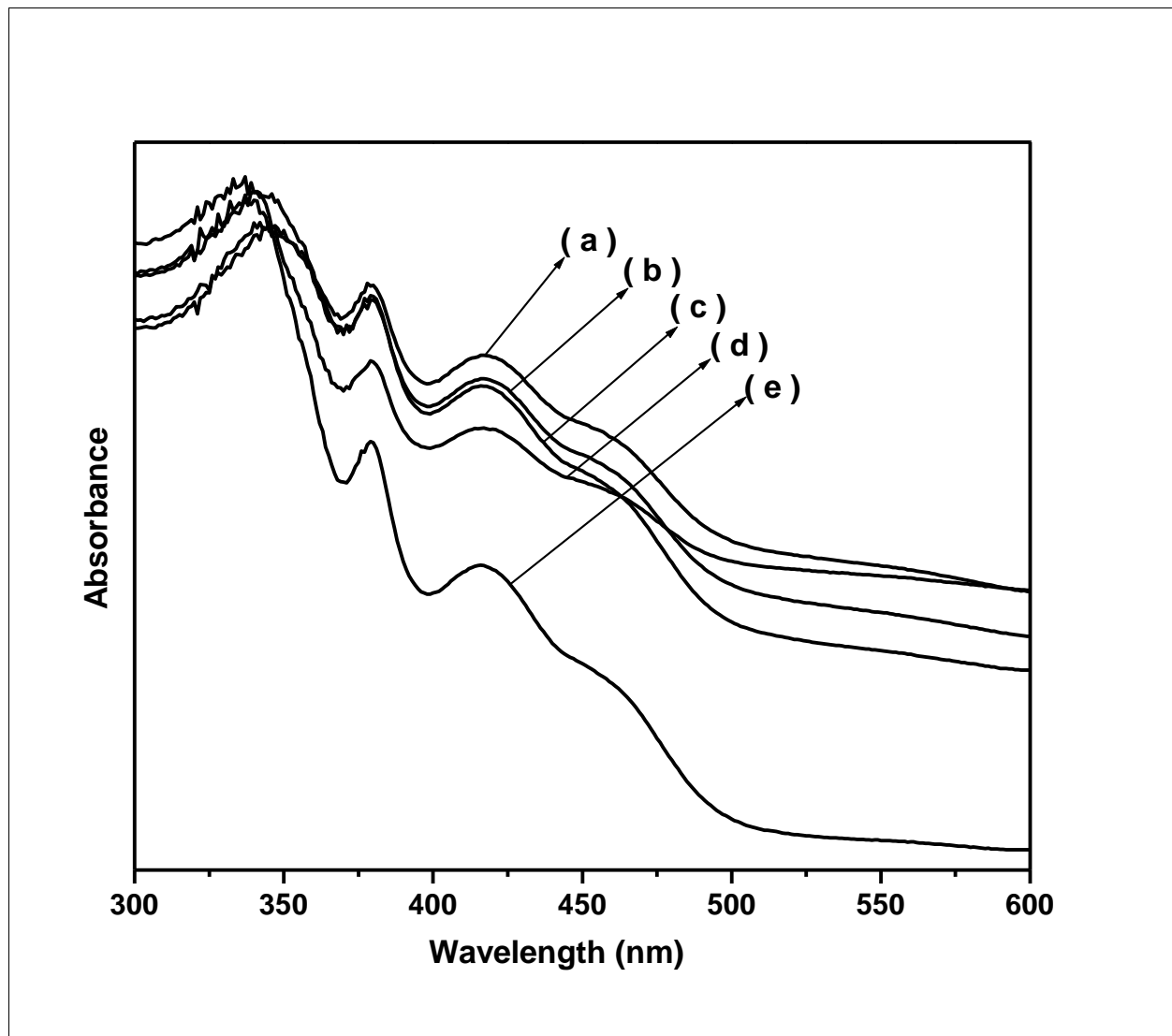


Figure 8. DRS spectra obtained on NiO nanoparticles prepared by colloidal thermal assisted reflux condensation method (a) without any surfactant (b) prepared with CTAB (c) prepared with PVP (d) prepared with PVA (e) & (f) prepared with SDS

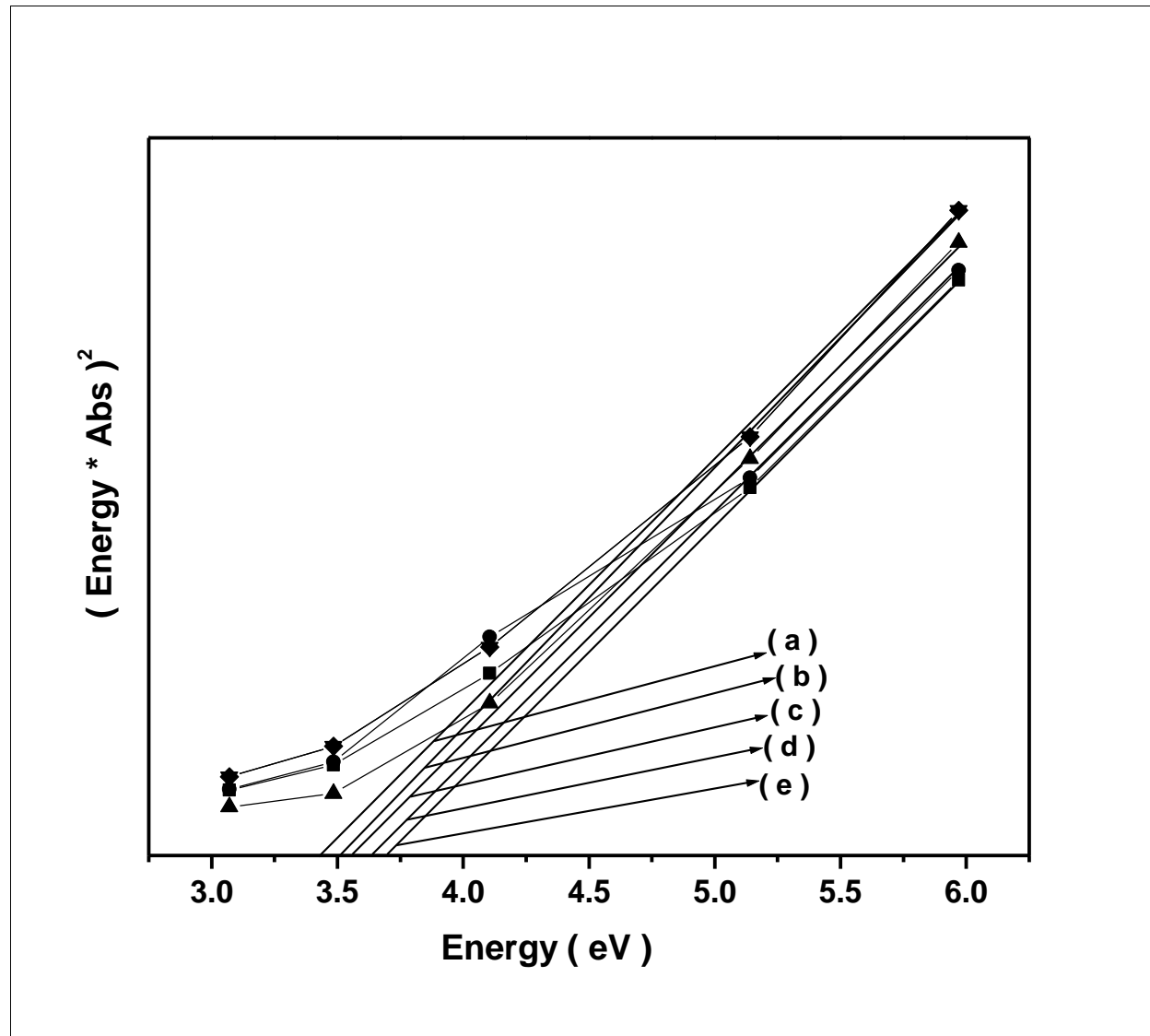


Figure 9. Band gap energy of NiO nanoparticles prepared by colloidal thermal assisted reflux condensation method
(a) without any surfactant (b) prepared with CTAB (c) prepared with PVP
(d) prepared with PVA (e) & (f) prepared with SDS

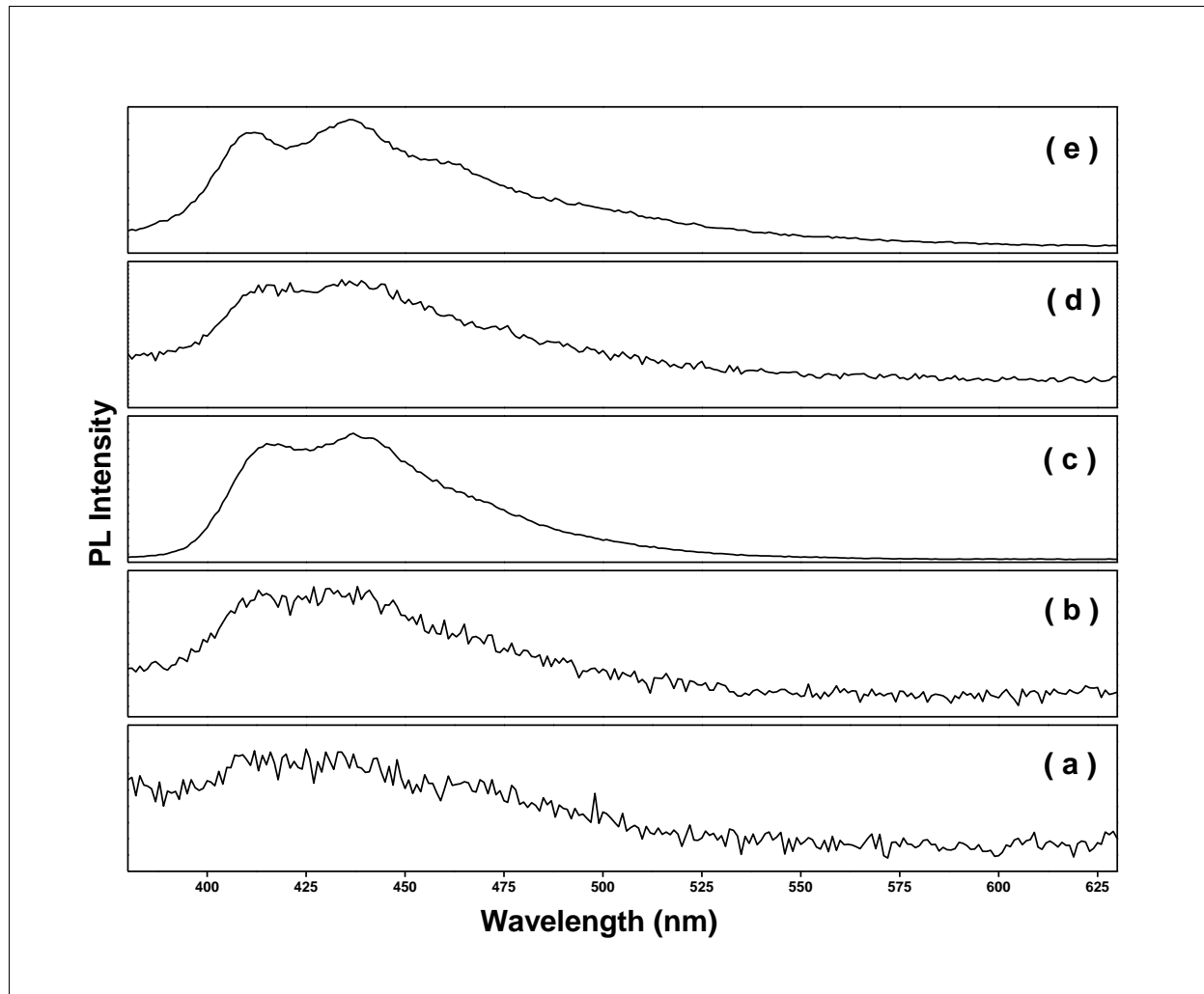


Figure 10. PL Emission spectra of NiO nanoparticles prepared by colloidal thermal assisted reflux condensation method (a) without any surfactant (b) prepared with CTAB (c) prepared with PVP (d) prepared with PVA (e) & (f) prepared with SDS

Table 2. Chemical composition data obtained on NiO (prepared by colloidal thermal assisted reflux condensation method) by EDAX analysis

Process	Atomic weight % of elements
Without any surfactant	Ni - 57.46 O - 42.54
CTAB	Ni - 53.0 O - 47.0
PVP	Ni - 45.91 O - 54.09
PVA	Ni - 46.07 O - 53.93
SDS	Ni - 45.91 O - 54.09

Table 3. Particle characteristics data obtained on NiO nanoparticles prepared by colloidal thermal assisted reflux condensation method

Process	Peak 1		Peak 2		Average particle size (nm)
	% Intensity	Diameter (nm)	% Intensity	Diameter (nm)	
Without any surfactant	91.1	319.5	8.9%	4830	329.4
CTAB	100	367.1	--	--	452.0
PVP	100	305.8	--	--	320.7
PVA	100	288.9	--	--	314.1
SDS	96.7	81.88	3.3	4760	78.98

6. References

- [1] Yang, J.L., Lai, Y.S., Chen, J.S., 2005. Effect of heat treatment on the properties of nonstoichiometric p-type nickel oxide films deposited by reactive sputtering. *Thin Solid Films*. 488, 242-246.
- [2] Sasi, B., Gopchandran, K.G., 2007. Nanostructured mesoporous nickel oxide thin films. *Nanotechnology*. 18, 115613-115621.
- [3] Bandara, J., Yasomance, J.P., 2007. P-type oxide semiconductors as hole collectors in dye sensitized solid-state solar cells. *Semicond. Sci. Technol.* 22, 20-24.
- [4] Miyata, T., Tanaka, H., Sato, H., Minami, T., 2006. P-type semiconducting Cu₂O-NiO thin films prepared by magnetron sputtering. *J. Mater. Sci.* 41, 5531-5537.
- [5] Na, D.M., Satyanarayana, L., Choi, G.P., Shin, Y.J., 2005. Surface morphology and sensing property of NiO-WO₃ thin films prepared by thermal evaporation. *Sensors*. 5, 519-528.
- [6] Avendano, E., Berggren, L., Niklasson, G.A., Granqvist, C.G., Azens, A., 2006. Electrochromic materials and devices brief survey and new data on optical absorption in tungsten oxide and nickel oxide films. *Thin Solid Films*. 496, 30-36.
- [7] Romana, C.K., Peter, B., 2006. Sol-Gel prepared NiO thin films for electrochromic applications. *Acta Chim. Slov.* 53, 136-147.
- [8] Lee K.D., Jung W.C., 2004. Effect of substrate temperature on the electrochromic properties and cyclic durability of nickel oxide films. *J. Korean. Phys. Soc.* 45(2) 447-454.
- [9] Kim, T. Y., Kim, J. Y., Lee, S. H., Shim, H. W., Lee, S. H., Suh, E. K., Nahma, K. S., 2004. Characterization of ZnO needle shaped nanostructures grown on NiO catalyst coated Si substrates. *Synthetic Metals*. 144(1), 61-68.
- [10] Wang, D. S., Xu, R., Wang, X., Li, Y. D., 2006. NiO nanorings and their unexpected catalytic property for CO oxidation. *Nanotechnology*. 17(4), 979-983.
- [11] Gondal, M. A., Sayeed, M. N., Seddigi, Z., 2008. Laser enhanced photocatalytic removal of phenol from water using p-type NiO semiconductor catalyst. *J. Hazardous Materials*. 155(1-2), 83-89.
- [12] Lampert, C.M., 2003. Large area smart glass and integrated photovoltaics. *Sol. Energy Mater. Sol. Cells*. 76, 489-499.
- [13] Bandara, J., Weerasinghe, H., 2005. Solid state dye sensitized solar cell with p-type NiO as a hole collector. *Sol. Energy Mater. Sol. Cells*. 85(3), 385-390.
- [14] He, J., Lindstrom, H., Hagfeldt, A., Lindquist, S.E., 1999. Dye sensitized nanostructured p-type nickel oxide film as a photocathode for a solar cell. *J. Phys. Chem. B*. 103, 8940-8943.
- [15] Taniguchi, A., Fujioka, N., Ikoma, M., Ohta, A., 2001. A development of nickel/metal-hydride batteries for EVs and HEVs. *J. Power Sources*. 100, 117-124.
- [16] Yoshimura, K., Miki, T., Tanemura, S., 1995. Nickel oxide electrochromic thin films prepared by reactive DC magnetron sputtering. *Jpn. J. Appl. Phys.* 34, 2440-2446.
- [17] Niklasson, G. A., Granqvist, C. G., 2007. Electrochromics for smart windows: Thin films of tungsten oxide and nickel oxide and devices based on these. *J. Mater. Chem.* 17(2), 127-156.
- [18] Hotovy, I., Rehacek, V., Siciliano, P., Capone, S., Spiess, L., 2002. Sensing characteristics of NiO thin films as NO₂ gas sensor. *Thin Solid Films*. 418(1), 9-15.
- [19] Wang, Y. G., Zhang, X. G., 2005. Enhanced electrochemical capacitance of NiO loaded on TiO₂ nanotubes. *J. Electrochem. Soc.* 152(4), A671-A676.
- [20] Krishnakumar, S.R., Liberati M., Grazioli, C., Veronese, M., Turchini, S., Luches, P., Valeri, S., Carbone, C., 2007. Magnetic linear dichroism studies of in situ grown NiO thin films. *J. Magnetism and Magnetic Materials*. 310, 8-12.
- [21] Li, F., Chen, H. Y., Wang, C. M., Hu, K. A., 2002. A novel modified NiO cathode for molten carbonate fuel cells, *J. Electroanalytical Chemistry*. 531(1), 53-60.
- [22] Kim, S. G., Yoon, S. P., Han, J., Nam, S. W., Lim, T. H., Oh, I. H., Hong, S. A., 2004. A study on the chemical stability and electrode performance of modified NiO cathodes for molten carbonate fuel cells, *Electrochimica Acta*. 49(19), 3081-3089.
- [23] Nagai, J., 1990. Advances in research and applications of electrochromic smart Windows. *Solid State Ionics* 40&41, 383-387.
- [24] Lee, K.D., 2001. Influence of film thickness on the chemical stability of electrochromic tungsten oxide film. *J. Korean Phys. Soc.* 38, 33-37.

- [25] Irwin, M.D., Buchholz, D.B., Hains, A.W., Chang, R.P.H., Marks, T.J., 2008. P-type semiconducting nickel oxide as an efficiency enhancing anode interfacial layer in polymer bulid heterojunction solar cells, Proceedings of the National Academy of Sciences. 105(8), 2783-2787.
- [26] Liu, K.C., Anderson, M.A., 1996. Porous nickel oxide/nickel films for electrochemical capacitors. 1996. J. Electrochem. Soc. 143, 124-130.
- [27] Srinivasan, V., J. W. Weidner, 1997. An electrochemical route for making porous nickel oxide electrochemical capacitors. J. Electrochem. Soc. 144, L210-L213.
- [28] Yu, G.H., Zeng, L.R., Zhu, F.W., Chai, C.L., Lai, W.Y., 2001. Magnetic properties and X-ray photoelectron spectroscopy study of NiO/NiFe films prepared by magnetron sputtering. J. Appl. Phys. 90, 4039-4043.
- [29] Hotovy, I., Buc, D., Hascik, S., Nennewitz, O., 1998. Characterization of NiO thin films by reactive sputtering. Vacuum 50, 41-44.
- [30] Nishizawa, S., Tsurumi, T., Hyodo, H., Ishibashi, Y., Ohashi, N., Yamane, M., 1997. Structural changes in ZnO/NiO artificial superlattices made by ion beam sputtering. Thin Solid Films. 302, 133-139.
- [31] Yoshimura, K., Miki, T., Tanemura, S., 1995. Nickel oxide electrochromic thin films prepared by reactive DC magnetron sputtering. Jpn. J. Appl. Phys. 34, 2440-2446.
- [32] Lin, Y., Xie, T., Cheng, B., Geng, B., Zhang, L., 2003. Ordered nickel oxide nanowire arrays and their optical absorption properties. Chem. Phys. Lett. 380, 521-525.
- [33] Dierstein, A., Natter, H., Meyer, F., Stephan, H.O., Kropf, C., Hempelmann, R., 2001. Electrochemical deposition under oxidizing conditions (EDOC): A new synthesis for nanocrystalline metal oxides. Scripta Materialia 44(8-9), 2209-2212.
- [34] Varkey, A.J., Fort, A.F., 1993. Solution growth technique for deposition of nickel oxide thin films. Thin Solid Films. 235, 47-50.
- [35] Xiang, L., Deng, X.Y., Jin, Y., 2002. Experimental study on synthesis of NiO nanoparticles. Scripta Materialia. 47, 219-224.
- [36] Wang, Y., Zhu, J., Yang, X., Lu, L., Wang, X., 2005. Preparation of NiO nanoparticles and their catalytic activity in the thermal decomposition of ammonium perchlorate. Thermochimica Acta. 437(1-2), 106-109.
- [37] Li, X., Zhang, X., Li, Z., Qian, Y., 2006. Synthesis and characteristics of NiO nanoparticles by thermal decomposition of nickel dimethylglyoximate rods. Solid State Communications. 137(11), 581-584.
- [38] Seike, T., Nagai, J., 1991. Electrochromism of 3d transition metal oxides. Sol. Energy Mater. 22, 107-117.
- [39] Sasi, B., Gopchandran, K.G., Monoys, P.K., Koshy, P., Rao, P.P., Vaidyan, V.K., 2002. Preparation and characterization of nanostructured NiO thin films by reactive pulsed laser ablation technique. Vacuum. 68, 149-154.
- [40] Beach, E.R., Shqae, K.R., Brown, S.E., Rozesveld, S.J., Morris, P.A., 2009. Solvothermal synthesis of crystalline nickel oxide nanoparticles. Mater. Chem. Phys. 115, 373-379.
- [41] Deki, S., Yanagimoto, H., Hiraoka, S., 2003. NH₃ terminated poly (ethylene oxide) containing nanosized NiO particles : synthesis, characterization, and structural considerations. Chem. Mater. 15, 4916-4922.
- [42] Puspharajah, P., Radhakrishna, S., Arof, A.K., 1997. Transparent conducting lithium doped nickel oxide thin films by spray pyrolysis technique. J. Mater. Sci. 32, 3001-3006.
- [43] Kamal, H., Elmaghraby, E.K., Ali, S.A., Abdel Hady, K., 2004. Characterization of nickel oxide films deposited at different substrate temperatures using spray pyrolysis. J. Cryst. Growth. 262, 424-434.
- [44] Wang, Y.D., Ma, C.L., Sun, X.D., Li, H.D., 2002. Preparation of nanocrystalline metal oxide powders with the surfactant mediated method. Inorg. Chem. Commun. 5, 751-755.
- [45] Surca, A., Orel, B., Pihlar, B., 1997. Sol gel derived hydrated nickel oxide electrochromic films: optical, spectro electrochemical and structural properties. J. Sol Gel Sci. Technol. 8, 743-749.
- [46] Park, J.Y., Ahn, K.S., Nah, Y.C., Shim, H.S., 2004. Electrochemical and electrochromic properties of Ni oxide thin films prepared by a sol gel method. J. Sol Gel Sci. Technol. 31, 323-328.
- [47] Lin, C., Al Muhtaseb, S. A., Ritter, J. A., 2003. Thermal treatment of sol gel derived nickel oxide xerogels. J. Sol Gel Sci. Technol. 28(1), 133-141.
- [48] Park, Y. R., Kim, K. J. 2003. Sol gel preparation and optical characterization of NiO and Ni_{1-x}Zn_xO Thin Films. J. Crystal Growth. 258(3-4), 380-384.
- [49] Sharma, P.K., Fantini, M.C.A., Gorenstein, A., 1998. Synthesis, characterization and

- electrochromic properties of NiO_xHy thin film prepared by sol gel method. *Solid State Ionics*. 113-115, 457-463.
- [50] Liu, K.C., Anderson, M.A., 1996. Porous nickel oxide/nickel films for electrochemical capacitors. *J. Electrochem. Soc.* 143, 124-130.
- [51] Coudun, C., Hocheplied, J.F., 2005. Nickel hydroxide stacks of pancakes obtained by the coupled effect of ammonia and template agent. *J. Phys. Chem. B* 109, 6069-6074.
- [52] Deng, X. Y., Chen, Z., 2004. Preparation of nano NiO by ammonia precipitation and reaction in solution and competitive balance. *Materials Letters*. 58(3- 4), 276-280.
- [53] Xin, X., Lu, Z., Zhou, B., Huang, X., Zhu, R., Sha, X., Zhang, Y., Su W., 2007. Effect of synthesis conditions on the performance of weakly agglomerated nanocrystalline NiO. *J. Alloys and Compounds*. 427(1- 2), 251-255.
- [54] Han, D. Y., Yang, H. Y., Shen, C. B., Zhou, X., Wang, F. H., 2004. Synthesis and size control of NiO nanoparticles by water in oil microemulsion. *Powder Technology*. 147(1-3), 113-116.
- [55] Sasi, B., Gopchandran, K.G, 2007. Preparation and characterization of nanostructured NiO thin films by reactive pulsed laser ablation technique. *Sol. Energy Mater. Sol. Cells*. 91, 1505-1509.
- [56] Liang, Z.H., Zhu, Y.J., Hu, X.L., 2004. β -nickel hydroxide nanosheets and their thermal decomposition to nickel oxide nanosheets. *J. Phys. Chem. B* 108(11), 3488-3491.
- [57] Chen, D.L., Gao, L., 2005. A new and facile route to ultrafine nanowires, super thin flakes and uniform nanodisks of nickel hydroxide. *Chem. Phys. Lett.* 405, 159-164.
- [58] Liu, X.H., Qiu, G.Z., Wang, Z., Li, X.G., 2005. Rationally synthetic strategy from nickel hydroxide nano sheets to nickel oxide nano rolls. *Nanotechnology*. 16, 1400-1405.
- [59] Parada, C., Moran, E., 2006. Microwave assisted synthesis and magnetic study of nano sized Ni/NiO material. *Chem. Mater.* 18, 2719-2725.
- [60] Alagar, M., Theivasanthi, T., Kubera Raja, A., 2012. Chemical synthesis of nano sized particles of lead oxide and their characterization studies. *J. Applied Sciences*. 12, 398-401.
- [61] Fu, Y.P. 2009. Electrical conductivity and magnetic properties of Li_{0.5}Fe_{2.5}Cr_{0.5}O₄ ferrite. *Mater. Chem. Phys.* 115(1), 334-338.
- [62] Dhandapandian, S., Gnanavel, B., Ramkumar, T., 2009. Utilization of granite and marble sawing powder wastes as brick materials. *Carpathian Journal of Earth and Environmental Sciences*. 4(2), 147-160.
- [63] Gnanachari, S. V., Bhat, R., Deshpande, R., Venkataraman, A., 2012. Synthesis and characterization of nickel oxide nanoparticles by self-propagating low temperature combustion method. *Recent Research in Science and Technology*, 4(4), 50-53.
- [64] Devi, B.S.R., Raveendran, R., Vaidyan, A.V., 2007. Synthesis and characterization of Mn²⁺ doped ZnS Nanoparticles. *Pramana*. 68, 679-687.

Nd:Yag Laser Ablation of Recuperated and Industrial Aluminum Alloys. Study of Threshold Ablation

Leila Baziz^b and Abdelkader Nouri^a

^a Department of Material Sciences, Univ. of Larbi Ben Mhidi, Oum El-Bouaghi (Algeria)

^b Department of physics, Univ. of Mila (Algeria)

Email: leila1_b@yahoo.fr

Received: 29 September 2013, accepted: 27 December 2013

Abstract

In this work, we used a nanosecond Nd: Yag laser ($\lambda=532$ nm) with a pulse duration of 15 ns, and an energy of 50 mJ and, therefore, we studied the threshold ablation of industrial aluminum alloy. The composition of the recuperated aluminum (% mass) is (72.02 Al, Si 13.05, 6.34 Zn, 4.28 O, 2.08 Mg, 1.75 Cu, 0.48 Ni) and the industrial aluminum is (83.10 Al, 1.66 Si, 4.12 Fe 2.17 O, 1.20 Mg, 5.47 Cu, 1.74 Mn, 1.79 Pb). For nanosecond lasers, the primary energy is lost by thermal diffusion in the irradiated target, because there is enough time to convert optical energy into thermal energy and heat spread. Fusion and / or evaporation may take place if the surface temperature exceeds the critical point when the energy of radiation is above the ablation threshold. The results shows that the threshold ablation of the recuperated aluminum is lower than that of the aluminum industry, it is about 5 J.cm² for the recovered aluminum and 10 J.cm² for the industrial aluminum. The threshold ablation is shifted towards the low values when the number of pulses increases.

Keywords: laser-matter interaction; Laser ablation; Aluminum Alloys

Introduction

Nanosecond laser pulses may produce both thermal melting (as femtosecond and picosecond pulses) or ultrafast nonthermal melting depending on the pulse fluence. This was demonstrated experimentally by Sokolowski-Tinten et al. [1], who found that the transformation of GaAs into its liquid state occurs within several tens of picoseconds at fluences close to the melt threshold due to thermal melting under highly superheated conditions [1] or within several hundred femtoseconds via carrier excitation[1, 2] for very high fluences. The processes occurring under high energetic fs pulse irradiation could be described more precisely with the help of the theoretical work of Stampfli and Bennemann [3]. The joining of very small metallic workpieces (10– 200 μ m) causes problems that often cannot be solved by conventional methods. In this case, soft soldering by means of laser radiation is sufficient. During soldering, laser light is used to melt an additional material with a considerably lower melting temperature than that of the material of the component to be joined. In order to understand this phenomenon, metallic alloys (Al, Cu, Zn, ...) are irradiated by a Nd:Yag pulsed laser. The chemical distribution of elements can be influenced, in particular the oxygen [4] as well as the microhardness [5]. The irradiated area is studied by the profilometer instrument in order to measure the ablation depth.

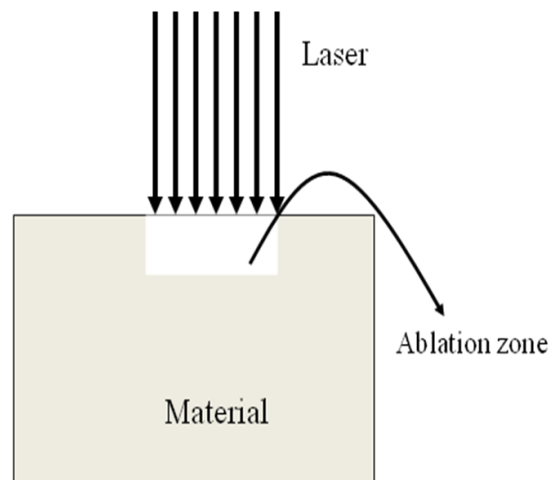


Fig.1. Schematic representation of ablation procedure

Experimental

The samples studied are two materials, industrial and recuperated aluminum alloys. They were polished mechanically and cleaned. The chemical composition of each type is obtained by X-ray analysis[4]. The chemical composition of recycled aluminum alloy is Al(72.02 wt %), Si(13.05 wt %), Zn(6.34 wt %), O(4.28 wt %), Mg(2.08 wt %), Cu(1.75 wt %), and Ni(0.48 wt %). The chemical composition of industrial aluminum alloy is Al(83.10 wt %), Cu(5.47 wt %), Fe(4.12 wt %), O(2.71 wt %), Mn(1.74 wt %), Si(1.66 wt %), and Mg(1.20 wt %). A

nanosecond pulsed laser (Nd:Yag) is used to irradiate an aluminum alloy sample (fig.1). The instrument used in this experiment is the Spectrum laser system. The pulse duration, wavelength, and pulse energy are 15 ns, 532 nm, and 50 nJ, respectively. All irradiation experiments are performed in air at room temperature. The analysis of irradiated area is realized by the profilometer instrument in order to measure the ablation depth. The properties of material studied are reported in the table 1.

Table1: Main properties of the two alloys studied (compared with pure Aluminum)

	recuperated aluminum	industrial aluminum	pure Aluminum
Density	2816	2614	2700
Microhardness (kg F/mm ²)	118	125	2.75
Thermal conductivity (W/m.K)	128	160	237

Results

The fluence threshold ablation (F_s), by definition, is the influence filed in the material from which a significant removal is achieved [1, 2]. The fluence threshold depends on the material and laser parameters[1]. The fluence threshold ablation may be shortened to one critical temperature to be reached for a regime ablation [3]. It is measured experimentally by extrapolating the quasi-linear evolution of the ablation depth (or the quantity of material ejected) depending on the fluence; for the low fluences until the zero, the ablation depth is nil. Figure 2 (a) and (b) show the ablation depth as a function of fluence for the two studied alloys, recuperated and industrial aluminum respectively. The threshold ablation is around 7 J.cm⁻² for recuperated aluminum and 10 J.cm⁻² for the industrial aluminum. That depends on the number of pulses. The ablation threshold tends toward low values when the number of pulses increases (see fig.2 (a) and (b)) the tow cases, 80 and 40 pulses).

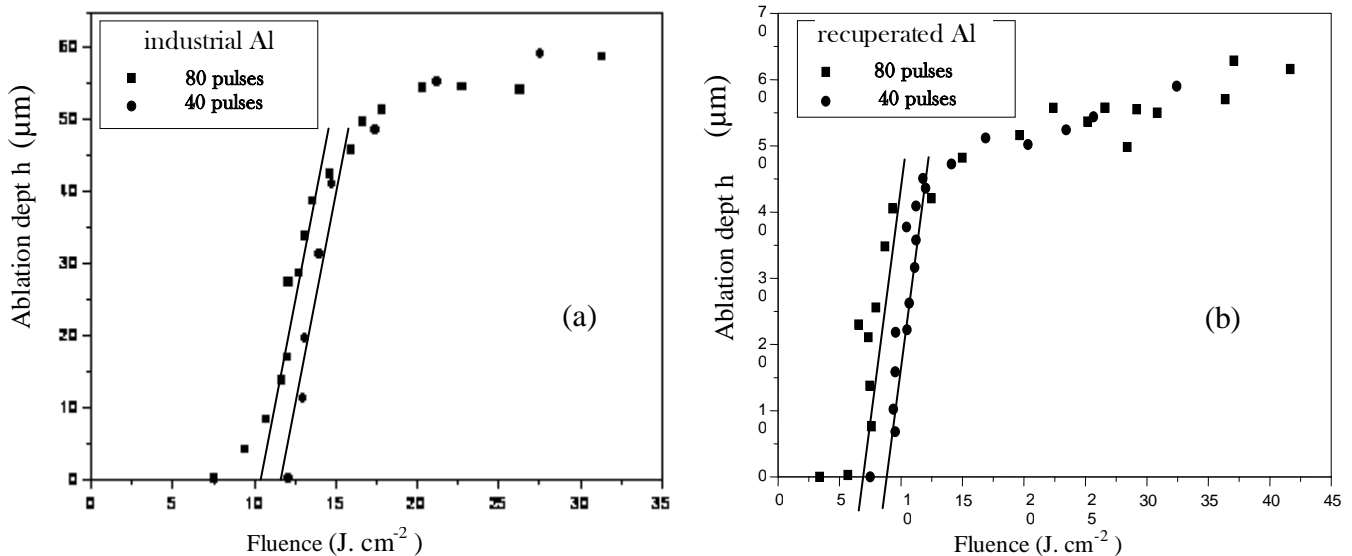


Fig.2. Dependence of ablation depth on fluence for industrial (a) and recuperated aluminum(b)

The threshold ablation in the industrial aluminum is greater than that one of the recuperated aluminum; this is may be due to the low thermal conductivity of the recuperated aluminum in comparison with that of the industrial aluminum. So, when the metal has a high thermal conductivity, thermal energy will be transported quickly within the sample, so it does not accumulate in the irradiated zone, leading to a ablation depth.

The quantity of ablated matter tends to saturation for high fluencies because the crater is very deep and because a quantity of laser energy is absorbed by plasma created near to the ablation zone.

Conclusion

The two studied alloys (industrial and recuperated aluminum) contain several chemical elements; each alloy is composed of more than six elements. So it is a complex material, and its interaction with a laser pulse of high intensity causes strange and very complex mechanisms. However, the behavior of these alloys in the ablation

procedure is similar to that for simple alloys (binary or ternary). The threshold ablation is about 10 J.cm^{-2} .

Références

- [1] J.C. Miller, R.F. Haglund, Laser ablation and Desorption, in: in: John C. Miller, R.F. Haglund Jr. (Eds.), Experimental methods in the physical science Vol 30. Academic Press, 1998, pp. 255-289
- [2] J. P. Dufour, M. Gerland, P. Darquey, Scripta metallurgica, Traitements de surface d'un alliage d'aluminium par des impulsions laser, 23(1989) 283-488.
- [3] L.V. Zhiligei, B.J. Garrison, Microscopic Mechanisms of Laser Ablation of Organic Solids in the Thermal and Stress Confinement Irradiation Regimes, J. Appl. Phys. 88, 3(2000) 1281-1298.
- [4] L. Baziz, A. Nouiri, and Y. A. Youcef, Influence of a Nanosecond Pulsed Laser on Aluminium Alloys: Distribution of Oxygen, Laser Physics, 16, 12(2006) 1643-1646.
- [5] L. Baziz, A. Nouiri, Treatment of commercial aluminum by Nd:YAG laser, J. New Tech. Mater., 01, 00(2011) 84-86.

Irradiance and temperature impact on thin film materials I-V curves

H. Haloui^{#1}, K.Touafek¹ and M. Zaabat²

¹Unité de Recherche Appliquée en Energies Renouvelables, URAER, Centre de Développement des Energies Renouvelables, CDER, 47133, Ghardaïa, Algeria.

²Laboratoire des composants actifs et matériaux, université d'Oum El Bouaghi, Algeria.

[#]haloui_h@uraer.dz

Received: 08 April 2013, revised: 24 December 2013, accepted: 27 December 2013

Abstract:

The thin-film solar cells are becoming increasingly used in various applications; this is mainly due to the continued high cost of mono or polycrystalline silicon. In addition, the thin film technology offers the most diverse applications including uses low solar irradiance. The main fields of thin film solar cells are: the chain of amorphous silicon (*a-Si*), the chain of cadmium telluride (*CdTe*) and chalcopyrite sector (*CIS* and *CIGS* material). In this paper, a study on the influence of light and temperature on the characteristics *I* (*V*) of different thin film photovoltaic cells (*a-Si:H* single, *a-Si:H* tandem *a-Si:H* tripple, *CdTe* and *CIS*) is detailed. Under standard conditions (illumination of 1000W/m^2 and cell temperature 25°C), we see that the *CdTe* is the closest that the monocrystalline silicon which has a maximum value of short circuit current material (3,26A).

Keywords: Thin films, Efficiency, Electricity, irradiance, temperature.

I. Introduction

Thin films are the second generation of photovoltaic technology, they have many applications in various areas such as optics, electronics, sensors in the photovoltaics technology. In this generation, there are three main channels:

A. die amorphous silicon (*a-Si*)

These cells are comprised of a glass substrate or plastic on which is deposited a thin layer of silicon [1], a process requiring very little energy. Although the performance of such cells is lower than crystalline cells (5-9%), which is due to the low mobility of charge carriers in these materials.

B. The die telluride of cadmium (*CdTe*)

It is a highly promising technology, allowing yields perfectly adequate (16.5%) in the laboratory. Share a bandgap of 1.5 eV perfectly adapted to the solar spectrum [2] and a very high absorption coefficient, only a layer of $2\ \mu\text{m}$ is necessary to obtain a very opaque material and absorbing a large part of the solar spectrum.

C. Chain chalcopyrite (*CIS* and *CIGS* material)

Selenium copper and indium (*CIS*) is a ternary material having a chalcopyrite structure. It has a coefficient of absorption between 100 and

1000 times greater than that of amorphous silicon. Cells based on chalcopyrite quaternary material such as *CIGS* (Cu for (Ga, In) (Se, S)) also has very interesting performance.

Production of such cells (thin film) is less expensive than the first generation (crystalline silicon) since it consumes less semiconductor material and does not require going through the step of converting the silicon "wafers". The problem of second-generation cells is lower efficiency of this cell type (6-7% and 14% in the lab for the amorphous silicon) and the toxicity of certain elements (cadmium) for their manufacture. However, this generation has many advantages for niche applications such as flexible modules, with low lights or high temperatures. Selenium and copper indium (*CIS*), which is at the stage of industrial production and offers a yield of 10 to 12% for its commercial modules does not present problems of toxicity of cadmium [3,4].

II. Modeling of thin film photovoltaic cell

The functioning of a photovoltaic cell is described by the "standard" model based on a single-diode (Figure 1), established by Shockley for a single PV cell and generalized for PV module by considering it as a set of identical cells connected in series / parallel [5, 6].

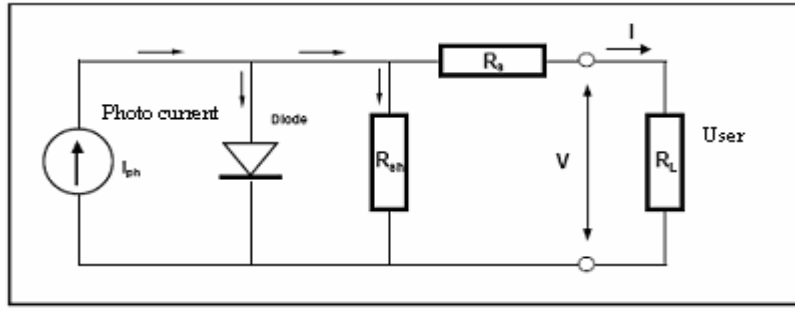


Figure 1: Equivalent circuit of a PV cell.

The current delivered by the panel is given by the following relationship [5]:

$$I = I_{ph} - I_0 \left[\exp \left(\frac{q \cdot (V + I \cdot R_s)}{N_{cs} \cdot \gamma \cdot k \cdot T_c} \right) - 1 \right] - (V + I \cdot R_s) / R_{sh} \quad (1)$$

With:

V: Voltage across the panel [V].

I_{ph} : Photo current [A], proportional to the irradiance, corrected by T_c .

I_0 : Current in diode means teme I_0 [exp (...) -1].

I: Diode reverse saturation current, temperature dependent [A].

R_s : serial resistance [Ω].

R_{sh} : shunt resistance (or parallel) [Ω].

Q: Electron charge = $1.602 \cdot 10^{-19}$ Coulomb.

k: Boltzmann's constant = $1.381 \cdot 10^{-23}$ J / K.

γ : Quality factor of the diode, typically between 1 and 2.

N_{cs} : Number of cells in series.

T_c : Effective temperature of cells [Kelvin].

The photocurrent I_{ph} varies with irradiance and temperature, we will determine relative to data values at reference conditions [5]:

$$I_{ph} = (\Phi / \Phi_{ref}) \cdot [I_{phref} + \mu_{ISC} \cdot (T_c - T_{Cref})] \quad (2)$$

Where:

Φ and Φ_{ref} : Effective and reference irradiance [W/m^2].

T_{Cref} and T_c : Temperature cell, reference and effective [K].

μ_{ISC} : Temperature Coefficient of photo current (or short circuit) [$A/^{\circ}K$].

The reverse saturation current of the diode is assumed I_0 vary with temperature according to the expression [5]:

$$I_0 = I_{0ref} \left(\frac{T_c}{T_{Cref}} \right)^3 \cdot \exp \left[\frac{q \cdot \mathcal{E}_G}{\gamma \cdot k} \left(\frac{1}{T_{Cref}} - \frac{1}{T_c} \right) \right] \quad (3)$$

Where \mathcal{E}_G : energy gap of the cell material (crystalline Si: 1,12 eV; amorphous silicon 1,7 eV CIS: 1,03 eV CdTe = 1,5 eV).

Reference conditions Φ_{ref} and T_{Cref} external conditions that are specified for the data used for model establishment. These are either the manufacturer's specifications, data always at STC

(“Standard Test Conditions” $1000W/m^2$, $25^{\circ}C$, AM1.5 spectrum) or values from in situ measurement module.

The model thus involves the following six unknown parameters: I_{phref} , I_{0ref} , γ , R_s , R_{sh} and μ_{isc} . The temperature coefficient of the photocurrent μ_{isc} is often given by the manufacturer and it is generally positive with a very low value (value/degree).

The value of the shunt resistance R_{sh} , represents the inverse of the slope of the plateau I (V) to V low. It can be easily determined from the measured data.

So we have four parameters (I_{phref} , I_{0ref} , γ , R_s) from the measurement of the characteristic I/V for a given pair (Φ_{ref} , T_{Cref}) reference conditions.

III. Simulation

In the previous section, we presented the basis of mathematical modeling of thin film PV modules. This model was developed under the matlab environment, then we simulated the characteristics I(V) for a wide range of variation of the illumination received by the photovoltaic panel (between 200 and $1000W/m^2$) for a constant temperature ($25^{\circ}C$) of the cell, and for a wide range of variation of cell temperature (from $25^{\circ}C$ to $70^{\circ}C$) for a fixed light ($1000W/m^2$). We applied the standard model to the different diode thin film photovoltaic modules (a-Si:H single, a-Si:H tripple, a-Si:H tandem, CdTe and CIS).

IV. Results and Discussions

The study of the influence of light on the characteristics I(V) for various photovoltaic modules (Figure 2) for a fixed cell temperature ($25^{\circ}C$) shows that increasing the illumination (from 200 to $1000W/m^2$) results in a displacement of the characteristic I=f(V) along the axis of the currents. The increase in the short circuit current is much greater than the open circuit voltage, since the short-circuit current is a linear function of illumination, whereas the open circuit voltage is logarithmic [7].

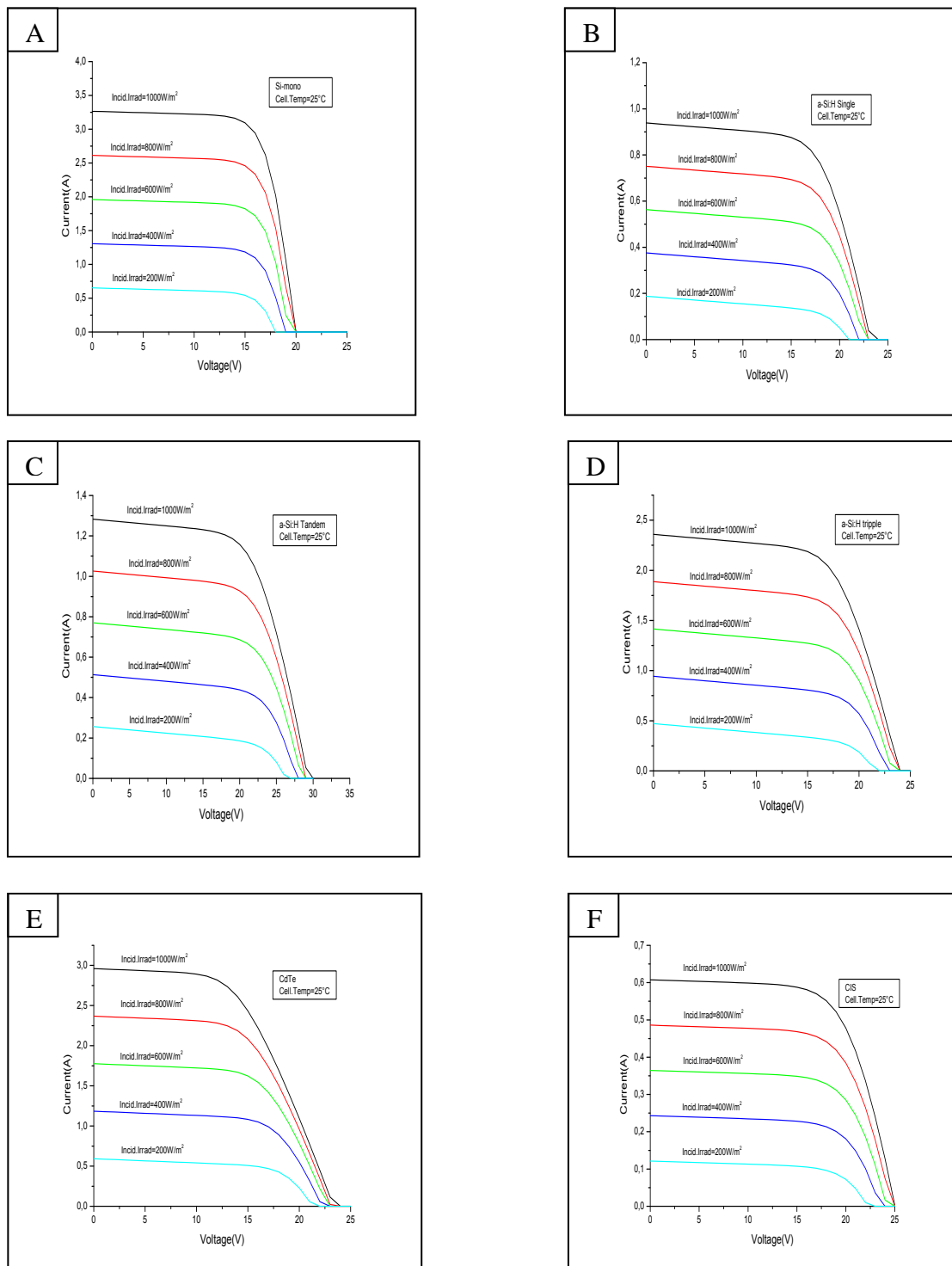


Figure 2: Changes characteristics I (V) as a function of the illumination for different modules:

(A) : Monocrystalline silicon module.

(B) :Module of a-Si:H single.

(C): Module of a-Si:H tandem.

(D): Module of a-Si:H tripple.

(E): Module of CdTe.

(F): Module of CIS.

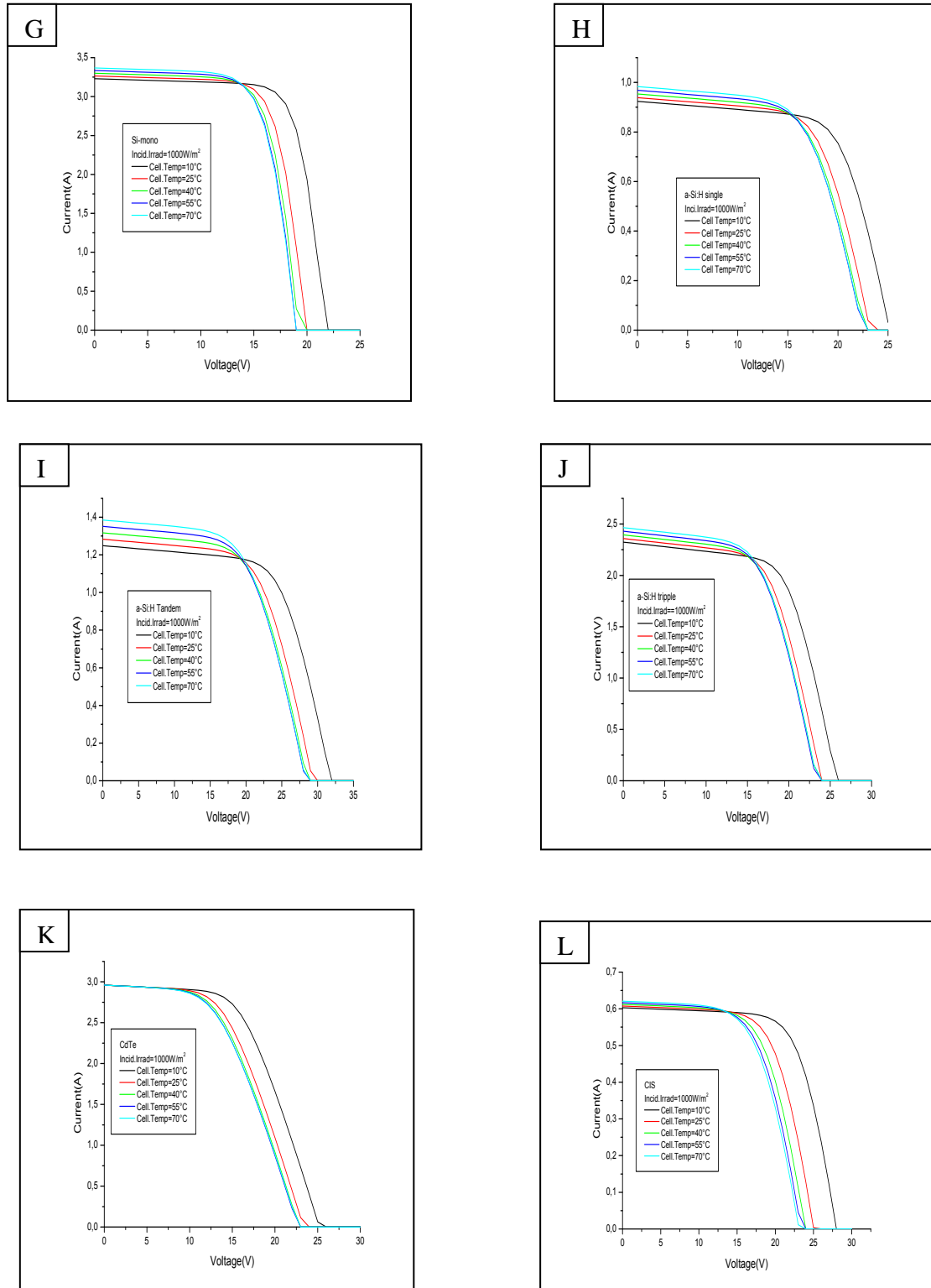


Figure 3: Changes characteristics I (V) as a function of temperature cell for different modules:
 (G): Monocrystalline silicon module.
 (H): Module of a-Si:H single.
 (I): Module of a-Si:H tandem.
 (J): Module of a-Si:H tripple.
 (K): Module of CdTe.
 (L): Module of CIS.

The study of the influence of the cell temperature on the characteristics $I(V)$ for various photovoltaic modules (Figure 3) for a fixed illumination ($1000\text{W}/\text{m}^2$) shows that increasing the cell temperature and also module temperature (from 10°C to 70°C), the Photo current I_{ph} also increases, this is due mainly to the decrease in the width of the band gap of the material. The forward current of the junction, but also increases and much faster resulting in a decrease of the open circuit voltage.

The results obtained (Figures 2, 3) show that in standard conditions (illumination of $1000\text{W}/\text{m}^2$ and a cell temperature of 25°C) the short circuit current reaches its maximum value (2.96 A) for the CdTe (Fig. 2E) and (2.36 A) for (a-Si:H tripple) (Fig. 2D), by against, it reaches minimum values for the a-Si:H single (0.94 A) (Fig. 2B) and CIS (0.61 A) (fig. 2F) and the a-Si:H tandem (1.28 A)(Fig. 2C). By comparison, one sees that the CdTe is the closest material that the monocrystalline silicon which has a maximum value of short circuit current (3.26 A) (Fig. 2A).

V. Conclusion

In this work, we introduced the electric model with a diode modules for various thin film (a-Si:H single, a-Si:H tandem a-Si:H tripple, CdTe and CIS) at different conditions sunshine and cell temperature.

The study of the effect of illumination on the characteristics $I(V)$ for different modules for a fixed cell temperature (25°C) shows that increasing

the illumination leads to an increase in short-circuit current, while the increase in cell temperature for a fixed illumination $1000\text{W}/\text{m}^2$ leads to an increase in short circuit current and a reduction in the open circuit voltage.

Under standard conditions (illumination of $1000\text{W}/\text{m}^2$ and cell temperature 25°C), we see that the CdTe is the closest that the monocrystalline silicon which has a maximum value of short circuit current material (3.26 A).

References

- [1] P.Pernet, Ph.D. Thesis, Ecole Polytechnic Federal Lausanne (2000).
- [2] J-C. Muller, Technical Engineering, BE 8579 folder.
- [3] L. El Chaar and al, Review of photovoltaic technologies, Renewable and sustainable energy reviews 15. P: 2165-2175 (2011).
- [4] Kamran Moradi and al, A review of PV/T technologies: Effect of control parameters, International journal of heat and mass transfer 64. P: 483-500 (2013).
- [5] André Mermoud, design and sizing of photovoltaic systems: introduction of thin film PV modules in the software PVsyst. Fund-GIS project CUEPE-NER, FINALREPORT, May 2005, www.cuepe.ch.
- [6] A.Mermoud. PVsyst: software for the study and simulation of photovoltaic systems. www.pvsyst.com, 1993-2005.
- [7] A. Yahya Ould Mohamed and al, Design and modeling of a photovoltaic generator, Journal of Renewable Energies Vol. 11 No. 3 (2008).